A rule-based multiscale model of hepatic stellate cell plasticity: critical role of the inactivation loop in fibrosis progression

Matthieu Bougueon[1,2], Vincent Legagneux[2], Octave Hazard [4,5], Jeremy Bomo[1,2], Anne Siegel[1], Jérôme Feret[3,4*] Nathalie Théret[1,2*],

1 Univ Rennes, Inria, CNRS, IRISA, UMR 6074, Rennes, France
2 Univ Rennes, Inserm, EHESP, Irset, UMR S1085, Rennes, France
3 Team Antique, Inria, Paris, France
4 DI-ENS (Inria, ÉNS, CNRS, PSL University), École normale supérieure, Paris, France
5 École Polytechnique, Palaiseau, France

* nathalie.theret@inserm.fr * jerome.feret@ens.fr

Abstract

Hepatic stellate cells (HSC) are the source of extracellular matrix (ECM) whose overproduction leads to fibrosis, a condition that impairs liver functions in chronic liver diseases. Understanding the dynamics of HSCs will provide insights needed to develop new therapeutic approaches. Few models of hepatic fibrosis have been proposed, and none of them include the heterogeneity of HSC phenotypes recently highlighted by single-cell RNA sequencing analyses. Here, we developed rule-based models to study HSC dynamics during fibrosis progression and reversion. We used the Kappa graph rewriting language, for which we used tokens and counters to overcome temporal explosion. HSCs are modeled as agents that present seven physiological cellular states and that interact with (TGFβ1) molecules which regulate HSC activation and the secretion of type I collagen, the main component of the ECM. Simulation studies revealed the critical role of the HSC inactivation process during fibrosis progression and reversion. While inactivation allows elimination of activated HSCs during reversion steps, reactivation loops of inactivated HSCs (iHSCs) are required to sustain fibrosis. Furthermore, we demonstrated the model's sensitivity to (TGFβ1) parameters, suggesting its adaptability to a variety of pathophysiological conditions for which levels of (TGFβ1) production associated with the inflammatory response differ. Using new experimental data from a mouse model of CCl4-induced liver fibrosis, we validated the predicted ECM dynamics. Our model also predicts the accumulation of iHSCs during chronic liver disease. By analyzing RNA sequencing data from patients with non-alcoholic steatohepatitis (NASH) associated with liver fibrosis, we confirmed this accumulation, identifying iHSCs as novel markers of fibrosis progression. Overall, our study provides the first model of HSC dynamics in chronic liver disease that can be used to explore the regulatory role of iHSCs in liver homeostasis. Moreover our model can also be generalized to fibroblasts during repair and fibrosis in other tissues.

Author summary

Chronic liver diseases (CLDs) are associated with the development of fibrosis which is characterized by an abnormal deposition of extracellular matrix (ECM) leading to severe liver dysfunction. Hepatic stellate cells (HSCs) are key players in liver fibrosis driving ECM remodeling. However numerous biological processes are involved including

HSC activation, proliferation, differentiation and inactivation and novel computational modeling is necessary to integrate such complex dynamics. Here, we used the Kappa graph rewriting language to develop the first rule-based model describing the HSCs dynamics during liver fibrosis and its reversion. Simulation analyses enabled us to demonstrate the critical role of the HSC inactivation loop in the development of liver fibrosis, and to identify inactivated HSCs as potential new markers of fibrosis progression.

Introduction

Liver fibrosis is an excessive wound healing response induced by chronic injuries, mainly caused by viral hepatitis (HCV, HBV), alcohol abuse and non-alcoholic steatohepatitis (NASH). Fibrosis is characterized by an accumulation of extracellular matrix (ECM) which increases the stiffness of tissues, leading to severe liver dysfunction. The final stage of fibrosis, cirrhosis, leads to complications such as ascites, variceal hemorrhage, encephalopathy and hepatocellular carcinoma, and is associated with a high mortality rate worldwide [1]. Activation of hepatic stellate cells (HSCs) is the main process underlying hepatic fibrosis [2]. In a normal liver, HSCs are quiescent, store vitamin A and are located in the Disse space between hepatocytes and endothelial cells that delineate sinusoids. Upon liver injury, HSCs are activated and transdifferentiate into ECM-secreting myofibroblasts (MFB) that contribute to tissue repair. In chronic liver disease, the inflammatory signal persists, leading to sustained HSC activation, ECM accumulation and fibrosis [2, 3, 4]. Importantly, reversibility or regression of liver fibrosis after elimination of the inflammatory agent has been observed in experimental models and clinical studies [5, 6]. This phenomenon is associated with the elimination of myofibroblasts, involving processes of apoptosis, senescence and inactivation, but the contribution of each of these mechanisms to the repair/fibrosis balance remains unclear.

Understanding the behavior of HSCs during liver injuries requires multiscale modeling approaches. Such approaches have been widely developed for modeling biological processes [7] and diseases [8, 9]. Because fibrosis is a pathological tissue repair activity that occurs in different organs, unified approaches have been proposed by including common components such as the inflammatory response and extracellular matrix remodeling [10]. However, each tissue is characterized by specific cell microenvironments. Different multiscale models have therefore been developed for cardiac [11] and pulmonary [12] fibrosis, and various approaches have been used to model the progression of liver fibrosis. Among them, the agent-based (ABM) multiscale model developed by Dutta-Moscato *et al.* successfully reproduced the experimental collagen deposition observed in carbon tetrachloride (CCl4)-induced fibrosis in rats. The model integrated parenchymal cells, inflammatory cells, collagen-producing cells and molecular regulatory agents, with rules defining the properties and interactions between all agents [13]. This model was then modified by preventing the migration of collagen-producing cells, thus providing a more accurate dynamic of collagen deposition [14]. The Dutta-Moscato model has also been extended and modified by Wand and Jiang [15] to include information about lipid accumulation induced by CCl4 treatment, making it possible to study the progression of liver fibrosis in presence or absence of steatosis. In addition to these agent-based models, Friedman and Hao recently published a partial differential equation (PDE) model for liver fibrosis that includes information on inflammation regulation and ECM remodeling, enabling exploration of anti-fibrotic drugs [16]. Although instructive, all these models reduce the dynamics of HSCs to their activation to become ECM-producing myofibroblasts, without taking into account the plasticity of HSCs recently illustrated by large-scale single-cell analyses. [17, 18, 19]. Among the complex behaviors of HSCs, the authors identified heterogenous

cell phenotypes such as proliferating cells and ECM-producing cells. In addition the inactivation processes remain poorly understood and information is lacking about the fate of inactivated HSCs (iHSCs) during liver fibrosis and reversion. The present study aims to decipher HSC dynamics by developing multiscale models which integrate for the first time all the HSC states during the development of fibrosis and its reversion. Using the Kappa rule-based formalism [20, 21, 22], our model describes the interactions between all cell populations and molecules such as transforming growth factor β 1 (TGFβ1) which induces HSC activation and promotes secretion of type I collagen, the major component of ECM [23]. We validated the predicted ECM dynamics using new experimental data from a mouse model of CCl4 induced liver fibrosis. Importantly, simulation studies demonstrated the regulatory role of HSC inactivation loops during liver fibrosis and predicted the accumulation of inactivated HSCs during chronic liver disease. By analyzing RNA sequencing data from 102 patients with non-alcoholic steatohepatitis (NASH) associated with liver fibrosis, we confirmed this accumulation, identifying iHSCs as novel markers of fibrosis progression.

Results

Three rules-based models for HSCs dynamics

We integrated information based on literature, to describe HSC dynamics during liver fibrosis and its reversion however the lack of some information led us to propose hypotheses and finally to develop three different models. As shown in Figure 1(A), the three models share common processes involving the different states of HSCs regulated by TGFβ1. In normal liver, HSCs are maintained in a non-proliferative quiescent state (qHSC) and store vitamin A. Upon liver injury (virus, toxic, etc.), the inflammatory response leads to the production of TGFβ1 which activates qHSCs into an activated state (aHSC). The fully activated HSCs are characterized by a myofibroblast (MFB) phenotype. Upon removal of liver injury, i.e in the absence of TGFβ1 in the models, MFBs are either eliminated through apoptosis and senescence pathways (apop_sene_MFB) or reverted to an inactivated HSC state (iHSC) close to but different from the quiescent state. Upon a new liver injury, i.e in the presence of TGFβ1 in the models, the iHSCs are reactivated (react_HSCs). In the same way that HSCs transform into MFBs, react_HSCs transform into reactivated MFBs (react_MFBs) however information is lacking about the fate of these cells. To overcome this issue, we developed two models in which the react_MFBs are either i) completely eliminated by the apoptosis/senescence pathways but not by inactivation, this model called *reactMFB-wo-inactivation* (wo for without) is described in Figure 1 A_1), or ii) eliminated in the same way as MFBs, i.e. by the apoptosis/senescence pathways and/or the inactivation pathway, this model called *reactMFB-with-inactivation* is described in Figure 1 A_2).

Similarly to react_MFB, information is lacking about the fate of iHSCs. While the activation of iHSCs by TGFβ1 has been described using *in vivo* and *in vitro* experiments [24, 25],no data have been reported about the fate of iHSCs in the absence of TGFβ1. However, Kisseleva *et al.* [24] showed a decrease in the iHSC population during the reversion process. We therefore developed a third model in which, in the absence of TGFβ1, iHSCs are either eliminated or return to a quiescent state, thereby participating in the repopulation of the injured liver with new qHSCs. This potential new source of qHSCs needs to be balanced with the self-renewal of native qHSCs in order to restore HSC homeostasis in the repaired liver. This model in which iHSCs revert to a quiescent state constitutes the third model called *iHSC-reversion-to-qHSC* which is illustrated in Figure 1 A_3.

Finally, we developed three models : *reactMFB-wo-inactivation*, *reactMFB-with-inactivation*, *iHSC-reversion-to-qHSC*. The biological processes of all the models have been integrated in Figure 1 B, where the interactions between TGFβ1 and aHSC, react_HSC, MFB and react_MFB cells leading to the induction of their proliferation and the production of COL1 are indicated.

The three models were built using the Kappa rule-based language (see Methods section) and simulations were performed using the KaSim tool [26] based on the Gillespie stochastic simulation algorithm (SSA) [27] . In these Kappa models, the hepatic stellate cells are the agents which are characterized by three sites (Figure 1 C) which are: i) the *cell_state* of HSCs (qHSC, aHSC, MFB, iHSC, react_HSC, react_MFB, apop_sene_MFB), ii) the *TGFB1_binding* that can be free or bound and iii) the state of the TGFβ1 receptor (*TGFBR*) that can be localized at the membrane, internalized or degraded. In addition to these agents, we introduced *counters* to scale the intermediate steps between cell states, and we used *tokens* to describe TGFβ1 and COL1 quantities instead of detailing the behavior of each molecule, thereby highly reducing the computational cost (see Methods section).

The resulting models respectively contain 75 rules and 41 parameters for model *reactMFB-wo-inactivation*, 76 rules and 43 parameters for model *reactMFB-with-inactivation* and 77 rules and 45 parameters for model *iHSC-reversion-to-qHSC*. These rules are grouped into 7 biological processes: 1) qHSC renewal, 2) binding of TGFβ1 to HSCs, 3) TGFBR dynamics, 4) HSC activation and differentiation, 5) HSC proliferation, 6) COL1 production and elimination and 7) MFB inactivation (detailed in Methods section).

Fig 1. Three models to describe HSC dynamics.
A1 Schematic representation of model *reactMFB-wo-inactivation* ; **A2** Model *reactMFB-with-inactivation* and **A3** model *iHSC-reversion-to-qHSC*. **(B)** Schematic representation of Kappa-modeled processes in all models. HSCs are agents characterized by seven cell physiological states (qHSC, aHSC, MFB, iHSC, apop_sene_MFB, react-HSC, and react_MFB). Rules describe the processes: (1) qHSCs are activated into aHSCs, (2) aHSCs are transformed into MFBs, (3) MFBs are transformed into apop_sene_MFBs to be eliminated, (4) MFBs are inactivated into iHSCs, (5) iHSCs are reactivated into react_HSCs upon TGFβ1 stimulation, (6) react_HSCs are transformed into react_MFBs. Similarly to MFBs, react_MFBs are eliminated by apoptosis and senescence (3) or by inactivation (4). (7) aHSCs and react_HSCs proliferate, (8) MFBs and react_MFBs proliferate, (9) aHSCs and react_HSCs produce COL1, (10) MFBs and react_MFBs produce COL1, (11) apop_sene_MFBs are degraded, (12) iHSCs are degraded. (13) qHSCs self-renewal. The effect of TGFβ1 is represented by gray arrows, it induces the activation of qHSCs, the reactivation of iHSCs, and the production of COL1 in aHSCs, react_HSCs, MFBs and react_MFBs. The reversion of iHSCs into qHSCs are represented by a dotted arrow. **(C)** Kappa contact map. HSCs are agents with three sites: *cell_state* (qHSC, aHSC, MFB, iHSC, react_HSC, react_MFB, apop_sene_MFB), *TGFB1_binding* (free or bound) and *TGFBR* (membrane, internalized or degraded).

Inactivation loops of react_MFBs are essential to maintain COL1 accumulation during chronic liver injury

To identify models that predict HSC behaviors and collagen accumulation that fits with the experimental data from Kiesseleva *et al.* [24], we conducted simulation studies using the protocol described by the authors for a mouse model of liver fibrosis and reversion, i.e. twice-weekly CCl4 (TGFβ1 in the model) injections for 8 weeks and an overall

reversion period of six months. Observations reported by Kisseleva *et al.* [24] included a 1.43-fold increase in cells expressing α-SMA and a $\sim$ 14-fold increase in the percentage of COL1 deposits at 8 weeks and a return to initial values at 6 months after the last injection. In addition, the authors assessed iHSCs/qHSCs ratios and identified a 50/50 distribution at one month and a total number of HSCs similar to initial conditions at six months of reversion. As shown in Figure 2, most qHSCs (98 %) were immediately activated upon the first stimulation of TGFβ1 across all models, a small number (2$\pm$1 %) of qHSCs persisting during the stimulation period. Activation of qHSCs led to the production of aHSCs that differentiated into MFBs. These cells express α-SMA protein, and we tracked α-SMA positive cells by summing the occurrences of aHSCs, MFBs, react_HSCs and react_MFBs. Note that even if the number of qHSCs and iHSCs is low, they can be activated or reactivated by TGFβ1 during repeated stimulation for two months. In line with this observation, Rosenthal *et al.* [28] recently suggested that iHSCs remain at a low level even during the activation phase. Comparison of the models showed that the react_MFB inactivation loop greatly affects model behavior. When inactivation of react_MFBs was not allowed (model *reactMFB-wo-inactivation*) Figure 2(A), we observed a lower amount of α-SMA expressing cells and of COL1 deposits than expected at 8 weeks, with amounts even decreasing before stimulation was stopped. Conversely, when inactivation of react_MFBs was allowed (model *reactMFB-with-inactivation*) Figure 2(B, C, D) we observed an accumulation of α-SMA expressing cells and COL1 deposits that varied according to the percentage of react_MFB inactivation. While 5% allows the model to fit with experimental observations (red circle in Figure 2), increasing the percentage to 10 and 50% led to higher amounts of α-SMA expressing cells (1.6- and 5-fold, respectively) and COL1 deposits (16- and 40-fold, respectively) at 8 weeks. Only the model with 5% of react_MFB inactivation led to a 50/50 distribution of the iHSCs/qHSCs ratio at one month and a return to the initial total number of cells at six months of reversion, as described in the experimental data [24].

Based on the model *reactMFB-with-inactivation* parameterized with 5% of react_MFB inactivation, we next evaluated the impact of a potential reversion of iHSCs to a quiescence state. As described in these new models *iHSC-reversion-to-qHSC*, we observed that regardless of the percentage of reversible cells, the overall behavior of the other model components was not affected (see S1 Fig).

Fig 2. Time-course analyses of cells and COL1 in models without or with react_MFB inactivation .
A series of simulations was performed using conditions of stimulation reported in Kisseleva *et al.* [24]. We used 10,000 TGFβ1 molecules per cell and 16 stimulations (twice a week) during 2 months. **A1** Model *reactMFB-wo-inactivation*. **B1** Model *reactMFB-with-inactivation* in which 5% of react_MFBs are inactivated. **C1** Model *reactMFB-with-inactivation* in which 10% of react_MFBs are inactivated. **D1** Model *reactMFB-with-inactivation* in which 50% of react_MFBs are inactivated. Stimulation of cells with TGFβ1 started on day 4 to allow the model to equilibrate. **A2**,**B2**,**C2** and **D2** display the variation in the number of cell occurrences for qHSCs, aHSCs, MFBs, iHSCs, react_HSCs, react_MFBs and α-SMA positive cells. The number of α-SMA cells is the sum of the number of aHSCs, MFBs, react_HSCs and react_MFBs. Data are expressed as the mean of 10 replicates. **A3**, **B3**, **C3** and **D3** display the variation of COL1 % area. Data are expressed as arbitrary unit (a.u) and all 10 replicates are represented. The red circles indicate the biological observations reported in [24]. The small circle is for an equal proportion of iHSCs and qHSCs at one month of recovery. The large circle is for the equality between the total number of cells at 6 months and the number of cells at T0.

Taken together, our data demonstrate that inactivation of react_MFBs is required to sustain COL1 accumulation by maintaining the level of α-SMA expressing cells, thus validating the model *reactMFB-with-inactivation*. Simulation analyses allowed us to determine that a 5% ratio between reac_MFB inactivation and apoptosis_senescence pathways reflected the cells and COL1 behaviors seen experimentally. Regarding iHSCs, our observations suggest that complete reversion of iHSCs to a quiescent state is a potential pathway to eliminate iHSC in the absence of TGFβ1. Since the outcome generated by the model *iHSC-reversion-to-qHSC*, in which iHSCs can revert to qHSCs was similar to the one obtained in the model *reactMFB-with-inactivation* (S1 Fig) we chose to retain the latter for the rest of the analyses.

Collagen I accumulation is sensitive to the dynamics of TGFβ1 stimulation

Our models are calibrated using experimental data from a mouse model of CCl4-induced fibrosis [24], a reproducible experimental model widely used to study fibrosis and repair [29]. Although the protocols vary somewhat in terms of the number, frequency and modalities of CCl4 injections, these experimental models induce similar liver fibrosis. Other models of induction of liver fibrosis in rodents have been developed, including injection of other chemical agents (such as thioacetamide (TAA) and dimethylnitrosamine (DMN)), high-fat diets and surgical interventions (such as bile duct ligation) [30, 31]. Whatever the etiology, induced damages lead to TGFβ1-dependent activation of HSCs, but with variable dynamics. It can happen very quickly in a model induced by CCl4 or slower in a model induced by a fatty diet. To explore the sensitivity of our model *reactMFB-with-inactivation*, we varied the concentration of TGFβ1 and the number and periodicity of stimulations. As shown in Figure 3, the model was highly sensitive to the amount of TGFβ1, but this sensitivity varied with the number of stimuli and periodicity, particularly for TGFβ1 values lower than 10,000 molecules per cell. Beyond that, the number of molecules exceeded the number of receptors per cell, and the model became saturated, as shown by the superposition of kinetic curves at 10,000 (green) and 100,000 (yellow) molecules per cell. At lower TGFβ1 levels, collagen accumulation was much more subtle. When stimulations were spaced sufficiently far apart, collagen levels returned to baseline and, remarkably, we observed a much stronger induction upon second stimulation, particularly at doses of 10,000 and 100,000 molecules per cell (Figure 3 A, periodicity 30 and 60 days). This induction of collagen 1 was less pronounced at low doses, but increasing the number of stimuli (Figure 3 B, periodicity 180 hours and 15 days) showed that collagen continues to accumulate with each new addition of TGFβ1 at the dose of 1000 molecules per cell, whereas it decreased for doses 10,000 and 100,000 molecules per cell. This effect remained visible for a larger number of stimulations (Figure 3C, periodicity 180h and 15 days and 3D, periodicity 90h and 180h).

Fig 3. Time course analysis of COL1 as a function of the variation in TGFβ1 concentration, number and periodicity of stimuli.
Results are expressed as the number of occurrences of COL1 according to the number of TGFβ1 stimuli: **(A)** 2, **(B)** 4, **(C)** 8, **(D)** 16, **(E)** 32, the periodicity which varies from 22.5 hours to 60 days and the concentration of TGFβ1: 10 (Red), 100 (Blue), 1,000 (Purple), 10,000 (Green) and 100,000 (Yellow) molecules per cell. The first stimulation occurs at day 4. Data are expressed as the mean of 5 iterations. P, Periodicity.

Model predictions validated by new experimental data in mice

To evaluate the model predictions, we analysed COL1 accumulation in a mouse model of CCl4 induced liver fibrosis. For the quantification of collagen deposits, we used second harmonic generation (SHG) microscopy which we have previously demonstrated to quantify fibrillar collagen in human [32] and mouse [33] livers. Note that the global evaluation of collagen deposits using Sirius red [24] and SHG microscopy may overestimate the contribution of HSCs since other cells can contribute to liver fibrosis such as portal fibroblasts and bone marrow-derived cells [34]. However, HSCs have recently been shown to be the exclusive source of myofibroblasts in CCl4-treated liver [35] which is why we chose data from CCl4-induced liver fibrosis to calibrate our model. As shown in Figure 4 A, we compared the signal quantification data obtained by SHG microscopy in our experimental model with the simulation data. Our experimental data showed maximum accumulation of collagen after 6 weeks and stabilization at a lower level at 8 and 10 weeks after treatment (Figure 4 A_1). In tissue samples from mice that have undergone the reversion protocol, the SHG signal shows a decrease in COL1 at 8 weeks after CCl4 removal (Figure 4 A_2). For the simulation studies, TGFβ1 parameters were adapted to the experimental protocol, i.e. three TGFβ1 stimuli in the first week and one stimulus per week for ten weeks. CCl4 induces rapid hepatocyte damages leading to inflammation and TGFβ1 production that we modeled using saturating TGFβ1 quantities (10,000 molecules/cell). As shown in Figure 4 B_1, the predicted curves for COL1 accumulation reached a maximum value similar to the experimental data, then at 8 and 10 weeks, the stabilization plateau was slightly higher in our simulation. Regarding the reversion protocol, the predicted curves for COL1 are in full agreement with the experimental data (Figure 4 B_2).

We also validated the prediction of COL1 dynamics using experimental data from other laboratories, including liver fibrosis models induced by dimethyl_nitrosamine [36] and thioacetamide [37]. Results are presented in (S2 Fig-A and B).

Fig 4. Comparison of model predictions and experimental data obtained in a mouse model of CCl4 induced liver fibrosis.
A1 Representative SHG microscopy images of collagen in mouse livers after 2, 4, 8 and 10 weeks of CCl4 treatment. **A2** For the reversion experiments, treatment was stopped at week 4. **A3** Collagen quantification was performed with ImageJ and results are expressed as percentage of SHG signal relative to total area (Mean ± SD). **B1**, Model simulations were performed using parameters corresponding to the CCl4 injection protocol (three TGFβ1 stimuli in the first week and one stimulus per week for ten weeks). Collagen accumulation was plotted and experimental data (from A1) are indicated with black bars. **B2**, Model simulations were performed using parameters corresponding to the reversion protocol (three TGFβ1 stimuli in the first week and one stimulus per week for 4 weeks). Collagen accumulation was plotted and experimental data (from A1) are indicated with blue bars.

iHSC accumulation is associated with human liver fibrosis

A major observation by Kisseleva et al. [24] is that the fibrotic response is exacerbated in mice that have undergone an initial chronic aggression followed by a reversion period allowing a return to a healthy tissue phenotype. This was associated with the presence of inactivated stellate cells (iHSCs) which display an enhanced response to TGFβ1 when stimulated in cell culture, leading to faster and greater production of COL1 [24, 25, 38]. These iHSCs would therefore still be present in the "repaired" liver after six months of reversion. To take this into account, we calibrated our model *reactMFB-with-inactivation* on Kisseleva 's observations *et al.* [24] after the second

aggression by introducing the hypothesis of a slow elimination of iHSCs. However, there is no experimental data describing the fate of these cells during aggression/reversion cycles. Using the relapse protocol described by Kisseleva *et al.*[24], we studied the behavior of iHSCs throughout injury-repair cycles. This protocol includes chronic injuries induced by eight CCl4 injections over one month, followed by a six-month recovery period, and then a new injury similar to the first. We repeated this cycle three times (Figure 5).

Our simulations show that the dynamics of α-SMA expressing cells and amounts of COL1 were consistent with Kisseleva's *et al.* experimental observations, i.e. higher levels of these two markers after the second aggression compared to the first one (Figure 5 A and B, cycles 1, 2). Importantly the model allowed us to detail the dynamics of iHSCs that was not experimentally evaluated and we observed an increased number of iHSCs (Figure 5 C, cycles 1, 2). When the aggression/reversion cycles were repeated, we showed an accumulation of iHSCs that was associated with that of (α-SMA expressing cells and COL1 (Figure 5 A,B, C, cycles 3, 4). The increased number of iHSCs may result from the balance between the higher number of α-SMA expressing cells leading to the inactivation of more iHSCs and the half-life of iHSCs. On the basis of these observations, the model predicts a progressive accumulation of iHSCs during cycles of aggression/reversion, suggesting a critical role for iHSCs in the dynamics of fibrosis, with accumulated iHSCs constituting a source of COL1 overproducing cells during reactivation.

Fig 5. iHSCs accumulate during injury-repair cycles.
Simulations were performed using repeated cycles comprising a first injury cycle (8 injections twice a week for 1 month), followed by a 6-month recovery period and a second injury cycle as previously described by Kisseleva *et al.* [24]. Data are expressed as the mean of 50 replicates for cells **(A)**, and all 50 replicates have been represented for COL1 **(B)** and iHSCs **(C)**.Overlaps are shown as grey area.

To validate this prediction, we searched for iHSC accumulation in samples from patients with liver fibrosis. To this end, we analyzed RNAseq data from a large multicenter study comprising 206 histologically characterized liver samples from patients with non-alcoholic fatty liver disease (NAFLD) including 102 patients with non-alcoholic steatohepatitis (NASH) associated with liver fibrosis [39]. Patients were divided in two groups : with low (F0-F1, n=34) and high (F3-F4, n=68) fibrosis grades. To identify iHSCs in human liver samples, we used an iHSC gene expression signature reported by Rosenthal *et al.* [28] in a mouse model of non-alcoholic steatohepatitis (NASH). This signature contained 39 genes that were significantly differentially expressed in iHSCs when compared to both qHSCs and aHSCs. In addition, we used 10 iHSC gene markers identified in a mouse model of CCl4-induced liver fibrosis [24] and validated in a *in vitro* reversion model of human activated cells [38]. The list of these genes is detailed in S1 Table.

As shown in Figure 6 A, gene set enrichment analyses (GSEA) using the signature identified by Rosenthal et al. [28] showed that iHSC genes were more expressed in the high fibrosis group than in the low fibrosis group (normalized enriched score=1.38, p-value=0.097). We performed a new analysis, adding the 10 marker genes identified by Kisseleva *et al.* and El Taghdouini *et al.* [24, 38] to the list of genes identified by Rosenthal *et al.*. As shown in Figure 6 B, this additional set of genes increased the statistical power of the GSEA analysis (normalized enriched score = 1.57, p-value = 0.048), confirming that the expression iHSC-specific genes is increased in patients with high fibrosis. These observations suggest the presence of an increased number of iHSCs during the progression of liver fibrosis, validating the predictions of our model.

Fig 6. iHSC accumulation is associated with liver fibrosis.
Gene set enrichment analyses of iHSC gene expression was performed in low fibrosis (F0-F1, n=34) and high fibrosis (F3-F4, n=68) samples from patients with non-alcoholic steatohepatitis (NASH) ([39]). **A**) Analysis performed with the iHSC gene signature identified by Rosenthal *et al.* [28]. **B**) Analysis performed with the iHSC gene signature identified by Rosenthal, supplemented by ten iHSC markers identified in [24, 38]. Results are presented in the form of correlation profiles between gene lists, enrichment scores (ES) which indicate to which phenotype (low or high fibrosis) the gene set is most positively correlated and heat maps visualizing clusters and gene distribution.

Discussion

Regardless of the underlying etiology, all chronic liver diseases are associated with the development of hepatic fibrosis, which is a major public health issue. Understanding the dynamics of hepatic fibrosis and its reversion is essential for the clinical management of patients and the adaptation of therapies. A pivotal process in the development of hepatic fibrosis is the TGFβ1-dependent activation of hepatic stellate cells whose plasticity is now widely recognized [40, 41]. Here, we investigated HSC plasticity by developing a multiscale model using a rule-based language. We provided the first model to describe the dynamics of HSCs during liver fibrosis and its reversion, demonstrating the importance of inactivated cells in these processes.

Kappa, a language adapted to multiscale modelling

While ordinary differential equations (ODEs)-based models have long been used to model biological dynamics, rule-based models (RBM) are much more appropriate for dealing with networks with combinatorial multi-state interactions as discussed by Chylek *et al.* [42]. Indeed, ODE approaches require the implementation of an equation for each species. ABM models, while more appropriate for bottom-up approaches than ODEs, require a description of all possible behaviors of agents including objects [43] or processes [44]. In the case of our model, the single agent has 4 sites, some of which have 8 or 14 different states. Using an ABM approach would have exploded the number of rules (~ 300) in the model to describe the 39 possible agent states. RBM approaches were therefore the most appropriate to represent the known interactions operating on stellate cells during fibrosis development and reversion. Based on site graph rewriting, BioNetGen [45] and Kappa [21, 22] are the two major languages used for RBM implementation and simulation.

Kappa formalism has been widely used for modeling biological reaction networks such as cell signaling [46], gene regulation [47], epigenetic regulation [48], repressilator system[49] and DNA repair [50]. Using Kappa language, our team previously developed a model to describe the regulatory role of extracellular matrix networks in TGFβ1 activation [51]. The transition from molecular to cell-molecule interaction models has been a new challenge, and we have recently demonstrated the applicability of the Kappa language in multi-scale modeling [52]. However, to overcome the explosion in memory demand due to the declaration of molecules and cells as agents, we have used *tokens* and *counters*. The way *tokens* are stored in memory considerably reduces the computational cost associated with the existence of different scales in the model. This involves the use of hybrid rules between agent and *token* whose applicability has been demonstrated in our model. *Counters* allowed a more detailed description of the activation and differentiation states of HSCs by creating intermediate steps and cell behaviors depending on their activation/differentiation stage, that better reflect experimental observations. Moreover, *counters* allow to model phenomena that the

duration of which is more predictable than chemical interactions. With time-exponentially distributed event, there is only one parameter: standard deviation which is fully characterised by the average time. Erlang distributions provides a mean to narrow the distribution hence leading to events which are more predictable (and which corresponds from a mathematical point of views to the composition of several atomic events following time-exponential distributions).

In short, *counters* and *tokens* are key to multiscale modelling in Kappa. *Tokens* enable a more compact representation of agent populations, *counters* enable a more compact representation of site populations, with both facilitating the search and abstraction of potential rule applications. To our knowledge, beside an unpublished model of pulmonary viral infection by William Waites [1], our study is the first one where *counters* and *tokens* have been used in a Kappa model.

A unique fibrosis model for different etiologies

While the role of TGFβ1 in HSC activation is well established, our model showed how its concentration, the number of stimuli and their periodicity influence the dynamics of liver fibrosis. These observations underline the adaptability of the model to the different pathophysiological conditions associated with the development of fibrosis. In murine models of liver fibrosis induced by chemical compounds such as CCl4, the toxic effect is massive, with strong hepatocyte necrosis, exacerbated inflammatory response and a saturating release of TGFβ1. In other models, such as diet-induced fibrosis, the immune response is different and fibrosis progresses more slowly. Sensitive to small variations in TGFβ1, our model reproduces the collagen accumulation observed in these different fibrosis mouse models. Similarly, the response to liver injury in human is etiology-dependent and may affect the dynamics of HSC activation. In contrast to chemical models, diet-induced fibrosis models developed to mimic the progression of NAFLD to non-alcoholic steatohepatitis (NASH) are characterized by a lower level of fibrosis. In addition, the dynamics of fibrosis are highly variable depending on the rodent strain and diet composition. Moreover, the optimal model of steatohepatitis leading to fibrosis (choline_deficient, amino_acid defined diet) is poorly reversible [61]. To overcome this heterogeneity, we chose a reversible diet model [62] which we compared with model predictions. We set the parameters of TGFβ1 to low levels (4500 molecules/cell, 6 stimuli and a periodicity of 14 days). As shown in supplementary Figure S2-C, the model captured the increase in COL1 but reversion dynamics were too fast, suggesting that for this condition the model requires additional regulators.

A model to capture stellate cell heterogeneity and microenvironment remodeling

Recent single-cell studies have demonstrated the great heterogeneity of HSCs and MFBs during the development of fibrosis [17, 28, 63]. These works also show that, in addition to a diversity of phenotypes, the dynamics of HSCs during their activation and differentiation process are far from linear, as shown by pseudotime analyses [64, 65]. Our approach manages to model this heterogeneity by introducing intermediate steps in the activation and differentiation process, and allowing cells in each of these states to proliferate, progress through the activation process and produce COL1. The implementation of these rules combined with the SSA algorithm (Stochastic Simulation Algorithm) means that, at each point in the simulation, there are different phenotypes and a 'unique' history is kept for each agent.

[1] https://git.sr.ht/ wwaites/immune-transmission

However, modelling HSC dynamics does not capture the full complexity of the microenvironment that governs these dynamics such as the multitude of events regulated by immune cells. Other multiscale models include the role of Kupffer cells in HSC activation via TNF-α [13, 15] or antagonistic regulation by M1 and M2 macrophages [16]. Similarly, it is difficult to include all the components involved in extracellular matrix remodeling. This process is finely regulated by the balance between the production of matrix metalloproteinases (MMPs) and their inhibitors, Tissue Inhibitor of metalloproteinases (TIMPs), both secreted by HSCs, MFBs, but also by immune cells involved in the resolution of fibrosis [66, 67, 68]. In their model, Friedman & Hao [16] reduced ECM remodeling to the sole contribution of macrophages and did not take into account the known role of HSCs at all. To overcome this molecular and cellular complexity while keeping remodeling process into our own model, we introduced *tokens* to represent low and high remodeling COL1. In this way we modeled both collagen accumulation during TGFβ1 stimulation and its regression upon TGFβ1 withdrawal.

Inactivation of reactivated MFBs, a critical factor in the progression of fibrosis

The process of inactivating HSC-derived MFBs has been presented as a key element in the reversion of fibrosis enabling the elimination of $\sim 50\%$ of MFBs [24, 25]. The authors have shown that the inactivated cells can be reactivated both *in vivo* and *in vitro* in response to a new stimulus, and that they are much more reactive and fibrogenic than initially activated cells [24, 38]. However, the fate of these reactivated cells remained unknown, leading us to hypothesize a potential re-inactivation of these reactivated cells. Our results showed that the inactivation of these cells was essential to maintain COL1 accumulation in chronic lesions, but that this inactivation had to be limited. Indeed, our models have shown that 5% of reactivated MFBs should be inactivated, experimental observations are no longer respected when using higher percentages of reactivated MFBs. This loop of inactivation and reactivation induces a change in the MFB population. As lesions accumulate, cells inactivated between aggressions are reactivated, resulting in a population of reactivated MFBs that becomes the majority and more fibrogenic cells. In support of these predictions, single-cell sequencing data identified these ECM-producing MFB phenotypes with increase fibrogenic activity [28].

Reversion of inactivated stellate cells to a quiescent state as an alternative to cellular elimination

Although the existence of iHSCs has been supported by several studies, their behavior is not yet well understood. These cells have a phenotype close to that of quiescent cells, but retain the memory of their previous activation [24, 38]. However, the fate of iHSCs in the absence of reactivation stimuli remains unknown. The development of our models enabled us to observe that the reversion of these iHSCs to a quiescent state, regardless of the percentage of cells affected, did not impact the overall behavior of the other components. This may be due mainly to the time required for the elimination of iHSCs and the renewal of quiescent cells, which is particularly slow in our models. This dynamic limits the impact of reversion. It is also possible that these cells have a faster elimination dynamic, but that this is compensated by a proliferation capacity, thus slowing down their elimination and increasing the impact of potential reversion. As it stands, our models suggest that the complete reversion of iHSCs to a quiescent state is a potential means of eliminating them in the absence of TGFβ1. Experimental follow-up of these cells over reversion times of more than one month would provide more

precise information on their fate.

Inactivated HSCs as new markers of fibrosis progression ?

The accumulation of iHSCs during fibrosis is a very important concept from a clinical perspective, as the progression of fibrosis is not at all linear. iHSCs within tissues could act as a kind of memory of an initial injury, making the tissue more sensitive to the next injury. Of course, this memory facilitates rapid repair, but the recurrence of these repair episodes, if too close together, accelerates the progression of fibrosis. Although our model is not fully adapted to follow the dynamics of the mouse NASH model due to the slow release of diet-induced TGFβ1, we showed that the observation of iHSC accumulation is validated in NASH patients with fibrosis.

Identifying inactivated cells *in vivo* would provide a genuine marker of patient history. However, this identification remains complex due to the intermediate phenotype of these cells, between quiescent and activated state. There is as yet no established phenotypic signature for inactivated cells, and gene expression signatures vary according to the mouse models used (NASH, CCl4). These phenotypic signatures depend both on the time of reversion and on the methods used to identify them, depending on whether their expression is compared with that of quiescent cells and/or activated cells. Recent advances in single-cell sequencing will enable us to refine these signatures by characterizing more specific groups of genes.

Conclusion

The present study provides two major findings. First we have demonstrated the applicability of the Kappa language to multi-scale approaches by using: *tokens*, to represent the quantities of molecules in a compact way, and *counters* to abstract the dynamics of cell-specific phenotypes. Second, we developed the first model of HSC dynamics during liver fibrosis and reversion. Thus, our model provides biological predictions for the reactivation loop, the dynamics of inactivated cells and their accumulation during fibrosis progression. These predictions have been validated either experimentally in a mouse model of CCl4-induced fibrosis, or using RNA sequencing data from patients with fibrosis.

Materials and methods

Kappa syntax

Kappa is a site graph rewriting language [69, 70, 71, 72] that uses a chemistry-inspired syntax to transparently describe the interactions between component occurrences. The syntax used by Kappa is that of site graphs, using rules to describe the behavior of agents over time. An agent describes species (e.g. cells, proteins) and defines the characteristics of these species. Rules define both the interactions between agents and their behavior. Agents are described by one or more *sites* which can have different *states*. These states allow agents to establish links between themselves. A rule describes a process that sets a condition (left-hand member) and an event (right-hand member). All the elements at the left of the $\rightarrow$ are the elements needed for the rule to be applied, the elements at the right are what will be produced. In the following example, two agents A and B interact to form a complex AB.

$$A(x\{p\},\ y[.]),\ B(y[.])\ \rightarrow\ A(x\{p\},\ y[1]),\ B(y[1])\ @\ 'k' \tag{1}$$

The agents A and B and their respective *sites* are written as : $agent_name(site_name\{state_value\}[binding_state])$. The agent A has its *site* x in a *state* p and its site y free ([.]), and the second agent B has it *site* y free. A and B will bind together via their *site* y. The symbol @ is followed by the expression that defines the rate of each potential application of the rule in the state of the system. That is to say the probability that a potential event effectively occurs within an infinitesimal interval of time.

In this study, we used *tokens* and *counters* to solve the computational problems associated with the specific task of multiscale modeling. *Tokens* constitute a pool of variables enabling the description of abundant molecular species in a continuous manner. Their use allows us to resolve the memory limitation caused by declaring molecular species as an agent. If a *token* such as ATP is added to the rule 1, the following rule is obtained (rule 2), where the binding of A and B requires ATP. What stands between | and @ defines the quantity of *token* to be deleted or added (2) when the rule is applied. Because the binding of A and B depends on the amount of ATP, the rate of the rule has to be modified to include the quantity of ATP, written as $|ATP|$.

$$A(x\{p\},\ y[.]),\ B(y[.])\ \rightarrow\ A(x\{p\},\ y[1]),\ B(y[1])\ |-10'ATP'@\ |ATP|*'\ k' \tag{2}$$

Similarly, with *counters*, we can use discrete interval to describe a special type of *site* which can be increased or decreased in the rules. In the following example (rule 3), A has a *site* called n, which is a *counter* that counts the number of bonds that can be formed by A during its lifetime in the system. This new rule allows A to bind to B as long as the value of n for A is greater or equal to one. When a bond is formed, the value of n decreases by one.

$$A(x\{p\},\ y[.], n\{\geq 1\}),\ B(y[.])\ \rightarrow\ A(x\{p\},\ y[1], n\{-=1\}),\ B(y[1])\ @\ 'k' \tag{3}$$

Modeling HSC dynamics

Using Kappa rules, we described HSC dynamics by including various biological processes such as the activation of quiescent HSCs (qHSC) by TGFβ1 leading to activated HSCs (aHSC), the transdifferentiation of aHSCs into Myofribroblasts (MFB), the elimination of MFBs after removal of TGFβ1 either by apoptosis and senescence pathways

(apop_sene_MFBs) or by reverting to an inactivated state (iHSC), the reactivation of iHSCs upon new TGFβ1 stimulation leading to reactivated HSCs (react_HSC) and the transdifferentiation of react_HSCs into reactivated MFBs (react_MFB). We also used rules to describe cell proliferation and production of collagen (except for qHSCs and iHSCs). In these models, HSCs are agents characterized by 3 *sites*: i) the cell state of HSCs (qHSC, aHSC, MFB, iHSC, react_HSC, react_MFB, apop_sene_MFBs), ii) the TGFB1 binding (free or bound) and iii) the state of the TGFβ1 receptor (TGFBR) that can be localized to the membrane, internalized or degraded. We introduced 2 *counters* to scale the intermediate steps between cell physiological states, and we used 4 *tokens* to describe TGFβ1 and collagen molecules. The resulting models contained 75 to 77 rules and 37 to 41 parameters depending on models. All rules are available in the GitHub repository: `https://github.com/MBougueon/HSC_model_Kappa`. We detailed here the representative rules of the biological processes. These rules are given in graphic form for easier reading.

qHSC renewal. qHSC renewal is modeled using two rules (Figure 7). These rules take into account the fact that the site *TGFB1_binding* on qHSCs must be *free*, since binding of TGFβ1 induces activation into proliferating HSC.

Fig 7. Renewal of quiescent HSCs.
An agent *HSC* with its site *cell_state* in a state *quiescent* and its site *TGFB1_binding* in a state *free* disappears (degradation). Conversely, the second rule describes the creation of this same agent. The rate of application of each rule is shown on the right.

TGFβ1 binding to cells. To describe the interaction of TGFβ1 with HSCs, 7 different rules are used according to the cell state. Figure 8 shows the binding rule of TGFβ1 to qHSCs. Only the site *cell_state* of the agent differs between these rules, except for MFBs and react_MFBs, where the rule rate is decreased. The fact that each agent can bind TGFβ1 introduces competition between agents for the binding of TGFβ1.

Fig 8. Binding of TGFβ1. Binding of TGFβ1 (as a token TGFB1_free) on the site *cell_state* of an *HSC* agent in a *quiescent* state, its *TGFB1_binding* site is in a *free* state and its *TGFBR* site is in a *Membrane* state. When the rule is fired, the value of the token *TGFB1_free* is decreased and the state of the site *TGFB1_binding* changes to *bound* and the state of the site *TGFBR* changes to *Internalized*.

Turnover of TGFBR. The endocytic pathways regulating *TGFBR* receptor signaling and turnover has been previously described by Di Guglielmo *et al.* [73] and modeled by Zi *et al.* [74]. During this process, TGFβ1 binding to TGFBR2 induces the recruitment of TGFBR1, leading to the activation of signaling pathways that regulate TGFβ1-dependent processes such as COL1 expression and cell proliferation. The trafficking of the TGFBR1/TGFBR2 complex between membrane and cytosol takes 30 min and is not affected by TGFβ1 binding. In the present study, we used *TGFBR* to represent the TGFBR1-TGFBR2 complex and we did not describe the intracellular signaling mechanisms. Upon TGFβ1 binding, the receptor *TGFBR* is internalized to transduce signals and can be either recycled (Figure 9 A) or degraded (Figure 9 B). To reduce model and time of calculation, the basal turnover of the receptor is not included in the absence of TGFβ1. To model TGFBR synthesis and localization to the membrane, a rule similar to the rule for degradation is used, changing the site *TGFBR* from the state *degraded* to *membrane*.

Fig 9. Degradation and recycling of the TGFβ1 receptor.
(**A**) The *TGFBR* site in an *Internalized* state changes into a *Membrane* state for the recycling rule, (**B**) and into a *Degraded* state for the degradation rule.

HSC activation and differentiation. During activation and differentiation, cells have the potential to proliferate and produce COL1 (in variable quantities depending on their activation and differentiation state). However, as each agent can only undertake one action at a time, different rules to describe cell activation, differentiation, proliferation and COL1 production are used.

To model HSC activation and differentiation into MFBs, *counters* are used ranging from 1 to 14, corresponding to the 14 days reported in *in vitro* experiments (1 to 7 corresponding to the change from qHSC to aHSC ; 8 to 14 corresponding to the changes from aHSC to MFB). On one hand, two rules describe the change of cell state (qHSC to aHSC and aHSC to MFB) and on other hand, two rules describe the step-by-step dynamics by increasing *counter intermediate_step* and decreasing *counter control_counter*.

Increasing the *counter intermediate_step* allows us to follow the activation and differentiation processes. The decrease of the *counter control_counter* ensures that the value of the *counter intermediate_step* remains in the range from 1 to 14. Figure 10 describes the dynamics of the activation, defined in 7 steps, corresponding to the seven days of the transition from qHSC to aHSC, with the implementation of a single rule. For the reactivation process, rules similar to those of the activation process were used.

Fig 10. HSC activation process. The rule specifies that as long as an agent *HSC*, whose site *cell_state* is in the state *activated* has its *counter control_counter* with a value lower than or equal to eight then, the value of its *counter control_counter* will be decremented by one and that of its *counter intermediate_step* will be incremented by one. This simple rule describes the seven stages of activation.

Cell Proliferation. A proliferation rule is written for each *counter* value. If an *HSC* agent proliferates, all the sites of the newly created agent will have the same value as those of the parent cell, except for TGFBR. Figure 11 shows an example of proliferation rules for the agent *HSC* whose site *cell_state* is in the *activated* state and its *counter intermediate_step* is equal to 7. The activation or differentiation steps do not affect the proliferation rate of agents and aHSCs and react_HSCs have additional rules for proliferation upon TGFβ1 binding. There are 30 rules to describe the proliferation process. The value of *state*, *intermediate_step* and *control_counter* is different between each rule to allow all cells to proliferate. Among these rules, 11 allow agents whose site *cell_state* is in the *aHSC* or *react_HSC* states to proliferate upon TGFβ1 stimulation by requiring the site $TGFB1_binding$ to be in a state *bound*, then transforming this site into a state *free* after the rule is fired.

Fig 11. Example of proliferation rules. For an agent *HSC* whose site *cell_state* is in the state *activated* and its *counter control_counter* equal to 7.

Collagen 1 turnover. The amount of COL1 in liver fibrosis and reversion results from the balance between production and degradation. Upon TGFβ1 stimulation, activated HSCs and MFBs are the major cell producing COL1 while apop_sene_MFBs contribute to the degradation of COL1 during fibrosis reversion [75, 76]. To overcome

the complex molecular mechanisms involved in regulation of COL1 degradation, COL1 was described using two different *tokens*: one for high remodeling ($COL1_remodeling_high$) and another for low remodeling ($COL1_remodeling_low$). These two *tokens* allow the description of the low degradation rate of COL1 during HSC activation and the high degradation rate during the process of reversion. COL1 dynamics is described using 12 rules: 8 for the production of $COL1_remodeling_high$ by aHSCs, MFBs, react_HSCs and react_MFBs in the presence and absence of TGFβ1 ; 2 for the degradation of each *token* ($COL1_remodeling_low$ being degraded at a slower rate than $COL1_remodeling_high$) and 2 to enable the two tokens to be linked (Figure 12 A). The transformation of $COL1_remodeling_high$ to $COL1_remodeling_low$ depends on the number of COL1-producing cells (aHSCs, react_HSCs, MFBs and react_MFBs) which are also characterized by expression of α-smooth muscle actin (αSMA).

The more cell agents are activated (or reactivated) and differentiated into MFBs (or react_MFBs), the greater the production of $COL1_remodeling_high$. A total of 8 rules describe the production of COL1. The state and the variable defining the amount of $COL1_remodeling_high$ is modified according to cells (Figure 12 B). Of these 8 rules, 4 are TGFβ1-free and 4 are TGFβ1-induced. For the latter 4, the cells must have the site $TGFB1_binding$ in a state *bound* and will be transformed into *free* after the production of $COL1_remodeling_high$.

Fig 12. Example of the rules involved in Collagen 1 turnover
A), Decrease of collagen degradation, the value of *token* $COL1_remodeling_high$ is decreased and that of $COL1_remodeling_low$ is increased ; **B**), Production of collagen by activated HSCs, the rate of application of the rule is proportional to the value of *counter intermediate_step*. This enables the cells furthest advanced in the activation process to produce more collagen than those just activated.

MFBs inactivation. After TGFβ1 removal, i.e. in the absence of TGFβ1 stimulation in the model, MFBs and react_MFBs are eliminated through the apoptosis and senescence pathways (Figure 13 A). An additional rule describes the process of elimination of apop_sene_MFB (not shown). The dynamics of the inactivation process is described in two steps using two rules (Figure 13 B). The first rule changes the MFBs to an inactivated cell state (iHSC) and decrements the counter value named *intermediate_step* to 0. The second rule increments the value of this same *counters* by 1 and increments the value of the *control_counters* by 13.

Fig 13. Rules for eliminating MFBs by apoptosis/senescence and inactivation.
A), The apoptosis/senescence rule consists of changing the site *cellular_state* of an agent *HSC* from a state *MFB* to *apoptosis_senescence*. **B**), For inactivation, two rules are necessary, the first changes the site *cellular_state* of an agent *HSC* from a state *MFB* to *inactivated* while reducing the value of the *counter intermediate_step* by 14. The second rule increases the values of *control_counters* by 13 and *intermediate_step* by 1.

Calibration and parameters estimation

For all the biological processes included in the models, 13 parameters were obtained directly from the literature, 9 were calculated and 22 parameters were estimated from biological observations by comparing model simulations with experimental data, running hundreds of simulations (S2 Table). Special attention was paid to calibrate

these 22 parameters because of the undocumented information about them, but also because of the interdependence between the parameters and the stochastic approach used. At certain points in the calibration of the model, some parameters were estimated empirically by groups (e.g. COL1 production, degradation and stabilization), leading to numerous simulations before finding the correct set of parameters. In addition, the behavior of iHSCs and reactivated MFBs remains unknown and we developed 3 different models taking into account different hypotheses : 1) model *reactMFB-wo-inactivation* where reactivated MFBs cannot be inactivated , 2) model *reactMFB-with-inactivation* were reactivated MFBs can be inactivated, 3) model *iHSC-reversion-to-qHSC* where iHSCs can revert into qHSCs, in the latter model the MFBs can be inactivated. Here we described the parameters based on biological observations. Note that the rule application rate is drawn according to an exponential distribution whose parameter is equal to the sum of the propensities of all the potential events in the system state. The rates of the rules must therefore be defined as the value $T_{1/2}$ of the biological process they describe.

.

Parameters for activation and differentiation rules. The activation process has been extensively documented using primary cultures of HSCs. Isolated qHSCs are spontaneously activated into aHSCs when cultured on plastic for 7 days, and complete transformation of qHSCs into MFBs takes place within 14 days, with a faster proliferation rate for aHSCs than for MFBs. [77, 78]. Based on these dynamics, the model was calibrated with 14 steps, and the proliferation rate of aHSCs was twice that of MFBs. *In vivo*, HSC activation is mainly driven by TGFβ1 which promotes proliferation and COL1 production. While qHSCs are highly sensitive to TGFβ1, MFBs are much less so [79, 78]. Consequently, we did not introduce rules for TGFβ1-dependent proliferation of MFBs in the model, and TGFβ1-dependent collagen production was five times lower in MFBs than in aHSCs.

Parameters for TGFβ-dependent rules. The kinetics of TGFβ1 binding to HSCs have already been reported using *in vitro* cell culture models [80] and a slower binding rate to MFBs has been described due to a decrease in the number of receptors [79]. The parameters of the receptor dynamics are those described by Vilar *et al.*[81] and the half-time required for TGFβ1 to induce a signal initiating the activation process was calculated using the model of Zi *et al.* [74]. This initialization step is necessary to activate the cellular machinery before the activation process begins. Note that this initialization time has been divided by 3.5 for iHSCs, as these cells are much more reactive than qHSCs in response to TGFβ1 [24, 25, 38]. Consistent with this, react_HSCs were allowed to proliferate immediately after being reactivated, whereas proliferation of aHSCs started at the third step of the activation process. This modeling choice was made to simulate the time required for qHSCs to initiate the cellular machinery of activation[82] whereas react_HSCs, due to their activation history, proliferated from the first step of their reactivation.

Parameters for qHSC self-renewal rate and iHSC elimination rules. In the absence of information on qHSC self-renewal rate and iHSC half-life, these parameters were estimated on the basis of data reported by Kisseleva *et al.* [24].

Parameters for MFB and react_MFB elimination rules. The half-life of MFBs and react_MFBs has not been documented, and was estimated on the basis of observations of the accumulation of these cells during TGFβ1 stimulation and their disappearance 1 to 2 months after the last TGFβ1 stimulation (Kisseleva *et al.*[24].

This accumulation represents an increase in the total number of HSCs after two months of CCl4 treatment from 10.6 to 14.3% the total liver cell population, where qHSCs and *alpha*-SMA cells account for 10.6% ($\pm$0.8) and 14.3% ($\pm$1.5), respectively.

Parameters for collagen 1 dynamic rules. The rules governing the production, degradation, stabilization, and destabilization of $COL1_high_remodeling$ and $COL1_low_remodeling$ were calibrated using data from Kisseleva *et al.* [24]. Since COL1 is experimentally quantified as deposits resulting from global remodeling, total COL1 (COL1_tot) is defined as the sum of $COL1_remodeling_high$ and $COL1_remodeling_low$. COL1_tot increased 12- and 14-fold after 1 and 2 months of TGFβ1 stimulation (two stimulation per week), respectively. aHSCs and react_HSCs produced 10 time less $COL1_remodeling_high$ than MFBs and react_MFBs. However, TGFβ1-dependent COL1 production was increased 10-fold in aHSCs and react_HSCs and only 2-fold in MFBs and react_MFBs, since aHSCs and react_HSCs are more sensitive to TGFβ1 [24, 25, 38]. In the absence of TGFβ1 stimulation, the model was calibrated to observe a rapid decrease in COL1_tot over the first month, followed by a gradual return to its initial value around 6 months later.

Parameters for the models *reactMFB-wo-inactivation* and *reactMFB-with-inactivation*

Upon removal of liver injury, *i.e.* in the absence of TGFβ1 stimulation in the model, 45% of MFBs are inactivated and the remaining 55% are eliminated through apoptosis and senescent pathways [83, 25]. iHSCs can be reactivated upon TGFβ1 stimulation to produce react_MFBs, but no information is available on their fate. Troeger *et al.* hypothesized that react_MFBs can undergo new inactivation/reactivation cycles, but should be limited for each cell [25]. Based on this hypothesis, two model families were created, including model *reactMFB-wo-inactivation* in which react_MFBs cannot be inactivated and model *reactMFB-with-inactivation* in which inactivation is possible. For the later, we developed models by varying the percentage of reactivated MFBs that could be inactivated from 1 to 50%.

Parameters for the model *iHSC-reversion-to-qHSC*

Using mouse models of liver fibrosis induced by CCl4, Kisseleva *et al.* [24] assessed the amount of iHSCs compared with qHSCs after removal of CCl4. They reported that qHSCs and iHSCs were in equal proportion after one month of recovery, and that the sum of qHSCs and iHSCs was equal to the initial number of qHSCs after six months of recovery. However, there is no information about the behavior of iHSCs in absence of CCl4 (i.e. of TGFβ1 in the models). In the absence of information on how iHSCs behave in the absence of CCl4 (i.e. TGFβ1 in the models), we developed models with a possible return to the quiescent state by varying the ratio of iHSC that transform into qHSC from 0 to 100%.

Experimental validation using a mouse model of CCl4-induced liver fibrosis

To validate the predictions of the model, collagen I was quantified during the course of fibrosis and reversion using a mouse model of CCl4 induced liver fibrosis. As previously described [84], seven-week-old female C57Bl/6 mice were treated with oral administration of CCl4 (Sigma-Aldrich, St. Louis, MO, USA) diluted in olive oil. A first dose of 2.4 g/kg of mouse weight was administered to mice three days before starting weekly treatment with a 1.6 g/kg dose for ten weeks. Control mice were treated

with the vehicle only (olive oil). Mice were sacrificed at 24 hrs after the last CCl4 dose. For fibrosis reversal experiments, mice were injected for 4 weeks with CCl4 and sacrificed at 8 days (1 week of recovery), or 15 days (2 weeks of recovery) after the last injection. Each group (control, fibrosis and reversion) at each time of sacrifice contained 5 mice. Collagen quantification was performed by SHG microscopy on 20 μm frozen tissue sections as previously described [85].

Computational validation using Gene set enrichment analysis of RNA-Seq data from patients with liver fibrosis

The enrichment for iHSC gene expression signature in human fibrotic samples was performed using Gene Set Enrichment Analysis (GSEA) [86, 87]. We used the iHSC gene expression signature previously identified by Rosenthal *et al.* [28] in a mouse model of non-alcoholic steatohepatitis (NASH) and we added iHSC markers previously identified in a mouse model of CCl4 induced liver fibrosis [24] and an *in vitro* reversion model of human activated HSCs [38]. The list of genes is detailed in supplementary S1 Table. For clinical samples, RNAseq data from patients with non-alcoholic fatty liver disease (NAFLD)[39] were used. Note that three genes (KRT20, GABRA3 and GSTT1) were not identified in the RNAseq data due to a low expression level. Liver samples with fibrosis were selected and separated in two groupss: with low (F0-F1, n=34) and high (F3-F4, n=68) fibrosis grade. RNAseq data were filtered using the BIOMART database [88] to select genes encoding proteins and data were normalized using DESeq2 [89] with a threshold of 100 reads. The filtration steps reduced the number of genes from 21,595 to 16,021.

Availability of the model

The 3 model files are available in the GitHub repository: `https://github.com/MBougueon/HSC_model_Kappa`. Using the KAPPA user interface downloadable from `https://kappalanguage.org/download`, the simulations can be performed by uploading the file of the model *HSC_dynamics_model.ka*. We used the version 4.2.12 of Kappa and 4.13.1 of OCaml (required to run Kappa).

Supporting information

S1 Fig. Temporal analysis of cells and COL1 in models with or without reversion of iHSC to a quiescent state. Simulation series were performed using conditions of stimulation from Kisseleva *et al.* [24]. TGFβ1 parameters were as follows 10,000 molecules per cell, 16 stimulation (twice a week) during 2 months. **(A1)**, model *reactMFB-with-inactivation* with 0% of the iHSCs reverting into qHSC, **(A2)** and **(A3)**, model *iHSC-reversion-to-qHSC* with 50% and 100% of the iHSCs reverting into qHSC, the remaining iHSCs being eliminated. **(B1, B2 and B3)**, variation in the number of cell occurrences for qHSCs, aHSCs, MFBs, iHSCs, react_HSCs, react_MFBs and α-SMA positive cells in the three models. The number of α-SMA cells is the sum of the number of aHSCs, MFBs, react_HSCs and react_MFBs. Data are expressed as the mean of 10 replicates. **(C1, C2 and C3)**, variation in the number of COL1 occurrence in the three models. Data are expressed as arbitrary unit (a.u) and all 5 replicates are represented.

S2 Fig. Comparison of model predictions and experimental data acquired in models of fibrosis induced by dimethyl_nitrosamine, thioacetamide and a high-fat diet. Simulations were carried out using the stimulation protocols described in the different models. **(A)** dimethyl_nitrosamine model: 3 TGFβ1 stimuli per week

for 6 weeks [36], **(B)** thioacetamide model: 2 simulations with TGFβ1 per week for 10 weeks [37], **(C)** high-fat model: 6 simulations with TGFβ1 every 14 days for 84 days, adapted to fit Farooq *et al.* results [62]. Collagen accumulation was plotted and experimental data from [36, 37, 62] are indicated with black cross.

S1 Table. List of the genes used for the Gene Set Enrichment Analysis. The first column contains the genes from Rosenthal *et al.*. It includes 39 genes that are differentially expressed in inactivated stellate cells compared with activated stellate cells and quiescent stellate cells [28]. The second list contains the eight marker genes of inactivated stellate cells identified both in a mouse model of CCl4-induced liver fibrosis [24] and in a *in vitro* reversion model of human activated cells [38].

S2 Table. Table of parameters. $A.U$: Arbitrary Unit corresponding to % areas of COL1 deposits, *Calculated*: parameter calculated directly from values found in the bibliography. *Estimated from biological observations*: parameters for which the values are estimated empirically in order to adapt the model to observations at a specific time. All the parameters describing a duration are calculated as the half-time of their reactions. Using the exponential law, the average dynamics of reactions corresponding to the experimental observations was ensured [90]

Acknowledgments

This work was supported by the Institut National de la Santé et de la Recherche Médicale (Inserm), the Institut national de recherche en informatique et en automatique (INRIA) and the University of Rennes. The authors thank the excellent support of the GenOuest bioinformatics core facility, Dr G Baffet and F Ezan for biological experiments and Dr C Lavau (Inserm U1085, University of Rennes) for proofreading the manuscript.

References

1. Sepanlou SG, Safiri S, Bisignano C, Ikuta KS, Merat S, Saberifiroozi M, et al. The global, regional, and national burden of cirrhosis by cause in 195 countries and territories, 1990-2017: a systematic analysis for the Global Burden of Disease Study 2017. Lancet Gastroenterol Hepatol. 2020;5(3):245–266.

2. Tsuchida T, Friedman SL. Mechanisms of hepatic stellate cell activation. Nat Rev Gastroenterol Hepatol. 2017;14(7):397–411.

3. Cordero-Espinoza L, Huch M. The balancing act of the liver: tissue regeneration versus fibrosis. J Clin Invest. 2018;128(1):85–96.

4. Kitto LJ, Henderson NC. Hepatic Stellate Cell Regulation of Liver Regeneration and Repair. Hepatol Commun. 2021;5(3):358–370.

5. Kisseleva T, Brenner D. Molecular and cellular mechanisms of liver fibrosis and its regression. Nature Reviews Gastroenterology & Hepatology. 2021;18(3):151–166.

6. Campana L, Iredale JP. Regression of liver fibrosis. In: Seminars in liver disease. vol. 58. Thieme Medical Publishers; 2017. p. 001–010.

7. Southern J, Pitt-Francis J, Whiteley J, Stokeley D, Kobashi H, Nobes R, et al. Multi-scale computational modelling in biology and physiology. Progress in biophysics and molecular biology. 2008;96(1-3):60–89.

8. Versypt ANF. Multiscale modeling in disease. Current opinion in systems biology. 2021;27:100340.

9. Gondal MN, Chaudhary SU. Navigating Multi-Scale Cancer Systems Biology Towards Model-Driven Clinical Oncology and Its Applications in Personalized Therapeutics. Frontiers in Oncology. 2021; p. 4767.

10. Amar MB, Bianca C. Towards a unified approach in the modeling of fibrosis: A review with research perspectives. Physics of life reviews. 2016;17:61–85.

11. Zeigler AC, Richardson WJ, Holmes JW, Saucerman JJ. Computational modeling of cardiac fibroblasts and fibrosis. Journal of molecular and cellular cardiology. 2016;93:73–83.

12. Leonard-Duke J, Evans S, Hannan RT, Barker TH, Bates JH, Bonham CA, et al. Multi-scale models of lung fibrosis. Matrix biology. 2020;91:35–50.

13. Dutta-Moscato J, Solovyev A, Mi Q, Nishikawa T, Soto-Gutierrez A, Fox IJ, et al. A multiscale agent-based in silico model of liver fibrosis progression. Frontiers in bioengineering and biotechnology. 2014;2:18.

14. Yoshizawa M, Sugimoto M, Tanaka M, Sakai Y, Nishikawa M. Computational simulation of liver fibrosis dynamics. Scientific reports. 2022;12(1):14112.

15. Wang Y, Jiang J. A two-dimensional (2d) systems biology-based discrete liver tissue model: A simulation study with implications for ultrasound elastography of liver fibrosis. Computers in biology and medicine. 2019;104:227–234.

16. Friedman A, Hao W. Mathematical modeling of liver fibrosis. Mathematical Biosciences & Engineering. 2016;14(1):143–164.

17. Krenkel O, Hundertmark J, Ritz TP, Weiskirchen R, Tacke F. Single cell RNA sequencing identifies subsets of hepatic stellate cells and myofibroblasts in liver fibrosis. Cells. 2019;8(5):503.

18. Terkelsen MK, Bendixen SM, Hansen D, Scott EAH, Moeller AF, Nielsen R, et al. Transcriptional Dynamics of Hepatic Sinusoid-Associated Cells After Liver Injury. Hepatology. 2020;72(6):2119–2133.

19. Payen VL, Lavergne A, Alevra Sarika N, Colonval M, Karim L, Deckers M, et al. Single-cell RNA sequencing of human liver reveals hepatic stellate cell heterogeneity. JHEP Rep. 2021;3(3):100278.

20. Boutillier P, Maasha M, Li X, Medina-Abarca HF, Krivine J, Feret J, et al. The Kappa platform for rule-based modeling. Bioinformatics. 2018;34(13):i583–i592.

21. Danos V, Laneve C. Graphs for core molecular biology. In: International Conference on Computational Methods in Systems Biology. Springer; 2003. p. 34–46.

22. Danos V, Laneve C. Formal molecular biology. Theoretical Computer Science. 2004;325(1):69–110.

23. Dewidar B, Meyer C, Dooley S, Meindl-Beinker AN. in Hepatic Stellate Cell Activation and Liver Fibrogenesis-Updated 2019. Cells. 2019;8(11).

24. Kisseleva T, Cong M, Paik Y, Scholten D, Jiang C, Benner C, et al. Myofibroblasts revert to an inactive phenotype during regression of liver fibrosis. Proc Natl Acad Sci U S A. 2012;109(24):9448–9453.

25. Troeger JS, Mederacke I, Gwak GY, Dapito DH, Mu X, Hsu CC, et al. Deactivation of hepatic stellate cells during liver fibrosis resolution in mice. Gastroenterology. 2012;143(4):1073–1083.

26. Danos V, Feret J, Fontana W, Krivine J. Scalable simulation of cellular signaling networks. In: Asian Symposium on Programming Languages and Systems. Springer; 2007. p. 139–157.

27. Gillespie DT. Exact stochastic simulation of coupled chemical reactions. The journal of physical chemistry. 1977;81(25):2340–2361.

28. Rosenthal SB, Liu X, Ganguly S, Dhar D, Pasillas MP, Ricciardelli E, et al. Heterogeneity of HSCs in a Mouse Model of NASH. Hepatology. 2021;74(2):667–685.

29. Scholten D, Trebicka J, Liedtke C, Weiskirchen R. The carbon tetrachloride model in mice. Lab Anim. 2015;49(1 Suppl):4–11.

30. Wu S, Wang X, Xing W, Li F, Liang M, Li K, et al. An update on animal models of liver fibrosis. Front Med (Lausanne). 2023;10:1160053.

31. Yanguas SC, Cogliati B, Willebrords J, Maes M, Colle I, van den Bossche B, et al. Experimental models of liver fibrosis. Arch Toxicol. 2016;90(5):1025–1048.

32. Gailhouste L, Le Grand Y, Odin C, Guyader D, Turlin B, Ezan F, et al. Fibrillar collagen scoring by second harmonic microscopy: a new tool in the assessment of liver fibrosis. J Hepatol. 2010;52(3):398–406.

33. Bourd-Boittin K, Bonnier D, Leyme A, Mari B, Tuffery P, Samson M, et al. Protease profiling of liver fibrosis reveals the ADAM metallopeptidase with thrombospondin type 1 motif, 1 as a central activator of transforming growth factor beta. Hepatology. 2011;54(6):2173–2184.

34. Iwaisako K, Brenner DA, Kisseleva T. What's new in liver fibrosis? The origin of myofibroblasts in liver fibrosis. J Gastroenterol Hepatol. 2012;27 Suppl 2(Suppl 2):65–68.

35. Yang W, He H, Wang T, Su N, Zhang F, Jiang K, et al. Single-Cell Transcriptomic Analysis Reveals a Hepatic Stellate Cell-Activation Roadmap and Myofibroblast Origin During Liver Fibrosis in Mice. Hepatology. 2021;74(5):2774–2790.

36. Sato Y, Yoneda A, Shimizu F, Nishimura M, Shimoyama R, Tashiro Y, et al. Resolution of fibrosis by siRNA HSP47 in vitamin A-coupled liposomes induces regeneration of chronically injured livers. J Gastroenterol Hepatol. 2021;36(12):3418–3428.

37. Abramovitch S, Dahan-Bachar L, Sharvit E, Weisman Y, Ben Tov A, Brazowski E, et al. Vitamin D inhibits proliferation and profibrotic marker expression in hepatic stellate cells and decreases thioacetamide-induced liver fibrosis in rats. Gut. 2011;60(12):1728–1737.

38. El Taghdouini A, Najimi M, Sancho-Bru P, Sokal E, van Grunsven LA. In vitro reversion of activated primary human hepatic stellate cells. Fibrogenesis & tissue repair. 2015;8(1):1–15.

39. Govaere O, Cockell S, Tiniakos D, Queen R, Younes R, Vacca M, et al. Transcriptomic profiling across the nonalcoholic fatty liver disease spectrum reveals gene signatures for steatohepatitis and fibrosis. Sci Transl Med. 2020;12(572).

40. Trivedi P, Wang S, Friedman SL. The Power of Plasticity-Metabolic Regulation of Hepatic Stellate Cells. Cell Metab. 2021;33(2):242–257.

41. Kordes C, Bock HH, Reichert D, May P, ussinger D. Hepatic stellate cells: current state and open questions. Biol Chem. 2021;402(9):1021–1032.

42. Chylek LA, Harris LA, Tung CS, Faeder JR, Lopez CF, Hlavacek WS. Rule-based modeling: a computational approach for studying biomolecular site dynamics in cell signaling systems. Wiley Interdiscip Rev Syst Biol Med. 2014;6(1):13–36.

43. Dematté L, Priami C, Romanel A. The BlenX Language: A Tutorial. In: Bernardo M, Degano P, Zavattaro G, editors. Formal Methods for Computational Systems Biology: 8th International School on Formal Methods for the Design of Computer, Communication, and Software Systems, SFM 2008 Bertinoro, Italy, June 2-7, 2008 Advanced Lectures. Berlin, Heidelberg: Springer Berlin Heidelberg; 2008. p. 313–365. Available from: `http://dx.doi.org/10.1007/978-3-540-68894-5$_$9`.

44. Ciocchetta F, Hillston J. Bio-PEPA: A framework for the modelling and analysis of biological systems. Theoretical Computer Science. 2009;410(33 – 34):3065 – 3084.

45. Harris LA, Hogg JS, Tapia JJ, Sekar JA, Gupta S, Korsunsky I, et al. BioNetGen 2.2: advances in rule-based modeling. Bioinformatics. 2016;32(21):3366–3368.

46. Danos V, Feret J, Fontana W, Harmer R, Krivine J. Rule-based modelling of cellular signalling. In: International conference on concurrency theory. Springer; 2007. p. 17–41.

47. Petrov T, Igler C, Sezgin A, Henzinger TA, Guet CC. Long lived transients in gene regulation. Theoretical Computer Science. 2021;893:1–16.

48. Krivine J, Danos V, Benecke A. Modelling Epigenetic Information Maintenance: A Kappa Tutorial. In: Bouajjani A, Maler O, editors. Computer Aided Verification. Berlin, Heidelberg: Springer Berlin Heidelberg; 2009. p. 17–32.

49. Wilson-Kanamori J, Danos V, Thomson T, Honorato-Zimmer R. Kappa rule-based modeling in synthetic biology. Methods Mol Biol. 2015;1244:105–135.

50. Köhler A, Krivine J, Vidmar J. A Rule-Based Model of Base Excision Repair. In: Mendes P, Dada JO, Smallbone K, editors. Computational Methods in Systems Biology. Cham: Springer International Publishing; 2014. p. 173–195.

51. Theret N, Feret J, Hodgkinson A, Boutillier P, Vignet P, Radulescu O. Integrative models for TGF-b signaling and extracellular matrix. Extracellular Matrix Omics. 2020; p. 209–225.

52. Bouguéon M, Boutillier P, Feret J, Hazard O, Théret N. The Rule-Based Model Approach: A Kappa Model for Hepatic Stellate Cells Activation by TGFB1. Systems Biology Modelling and Analysis: Formal Bioinformatics Methods and Tools. 2022; p. 69–126.

53. Glaser T, Baiocchi L, Zhou T, Francis H, Lenci I, Grassi G, et al. Pro-inflammatory signalling and gut-liver axis in non-alcoholic and alcoholic steatohepatitis: Differences and similarities along the path. J Cell Mol Med. 2020;24(11):5955–5965.

54. Gao B, Ahmad MF, Nagy LE, Tsukamoto H. Inflammatory pathways in alcoholic steatohepatitis. J Hepatol. 2019;70(2):249–259.

55. Schuster S, Cabrera D, Arrese M, Feldstein AE. Triggering and resolution of inflammation in NASH. Nat Rev Gastroenterol Hepatol. 2018;15(6):349–364.

56. Peiseler M, Schwabe R, Hampe J, Kubes P, lder M, Tacke F. Immune mechanisms linking metabolic injury to inflammation and fibrosis in fatty liver disease - novel insights into cellular communication circuits. J Hepatol. 2022;77(4):1136–1160.

57. Nishitsuji H, Funami K, Shimizu Y, Ujino S, Sugiyama K, Seya T, et al. Hepatitis C virus infection induces inflammatory cytokines and chemokines mediated by the cross talk between hepatocytes and stellate cells. J Virol. 2013;87(14):8169–8178.

58. Fairfax K, Nascimento M, Huang SC, Everts B, Pearce EJ. Th2 responses in schistosomiasis. Semin Immunopathol. 2012;34(6):863–871.

59. Wynn TA, Thompson RW, Cheever AW, Mentink-Kane MM. Immunopathogenesis of schistosomiasis. Immunol Rev. 2004;201:156–167.

60. Yokoyama H, Masaki T, Inoue I, Nakamura M, Mezaki Y, Saeki C, et al. disease. Heliyon. 2019;5(2):e01231.

61. Wei G, An P, Vaid KA, Nasser I, Huang P, Tan L, et al. Comparison of murine steatohepatitis models identifies a dietary intervention with robust fibrosis, ductular reaction, and rapid progression to cirrhosis and cancer. Am J Physiol Gastrointest Liver Physiol. 2020;318(1):G174–G188.

62. Farooq M, Hameed H, Dimanche-Boitrel MT, Piquet-Pellorce C, Samson M, Le Seyec J. Switching to Regular Diet Partially Resolves Liver Fibrosis Induced by High-Fat, High-Cholesterol Diet in Mice. Nutrients. 2022;14(2).

63. Zhang W, Conway SJ, Liu Y, Snider P, Chen H, Gao H, et al. Heterogeneity of hepatic stellate cells in fibrogenesis of the liver: insights from single-cell transcriptomic analysis in liver injury. Cells. 2021;10(8):2129.

64. Trapnell C, Cacchiarelli D, Grimsby J, Pokharel P, Li S, Morse M, et al. The dynamics and regulators of cell fate decisions are revealed by pseudotemporal ordering of single cells. Nature biotechnology. 2014;32(4):381–386.

65. Street K, Risso D, Fletcher RB, Das D, Ngai J, Yosef N, et al. Slingshot: cell lineage and pseudotime inference for single-cell transcriptomics. BMC Genomics. 2018;19(1):477.

66. Koda Y, Teratani T, Chu PS, Hagihara Y, Mikami Y, Harada Y, et al. CD8+ tissue-resident memory T cells promote liver fibrosis resolution by inducing apoptosis of hepatic stellate cells. Nature communications. 2021;12(1):4474.

67. Ramachandran P, Pellicoro A, Vernon MA, Boulter L, Aucott RL, Ali A, et al. Differential Ly-6C expression identifies the recruited macrophage phenotype, which orchestrates the regression of murine liver fibrosis. Proc Natl Acad Sci U S A. 2012;109(46):E3186–3195.

68. Duffield JS, Forbes SJ, Constandinou CM, Clay S, Partolina M, Vuthoori S, et al. Selective depletion of macrophages reveals distinct, opposing roles during liver injury and repair. J Clin Invest. 2005;115(1):56–65.

69. Danos V, Laneve C. Formal molecular biology. Theoretical Computer Science. 2004;325(1):69–110.

70. Faeder JR, Blinov ML, Goldstein B, Hlavacek WS. Rule-based modeling of biochemical networks. Complexity. 2005;10(4):22–41. doi:10.1002/cplx.20074.

71. Andrei O, Kirchner H. A Rewriting Calculus for Multigraphs with Ports. Electr Notes Theor Comput Sci. 2008;219:67–82.

72. John M, Lhoussaine C, Niehren J, Versari C. Biochemical Reaction Rules with Constraints. In: Programming Languages and Systems - 20th European Symposium on Programming, ESOP 2011, Held as Part of the Joint European Conferences on Theory and Practice of Software, ETAPS 2011, Saarbrücken, Germany, March 26-April 3, 2011. Proceedings. vol. 6602 of Lecture Notes in Computer Science. Springer; 2011. p. 338–357. Available from: `http://dx.doi.org/10.1007/978-3-642-19718-5`.

73. Di Guglielmo GM, Le Roy C, Goodfellow AF, Wrana JL. Distinct endocytic pathways regulate TGF-b receptor signalling and turnover. Nature cell biology. 2003;5(5):410–421.

74. Zi Z, Feng Z, Chapnick DA, Dahl M, Deng D, Klipp E, et al. Quantitative analysis of transient and sustained transforming growth factor-β signaling dynamics. Molecular systems biology. 2011;7(1):492.

75. Krizhanovsky V, Yon M, Dickins RA, Hearn S, Simon J, Miething C, et al. Senescence of activated stellate cells limits liver fibrosis. Cell. 2008;134(4):657–667.

76. Schnabl B, Purbeck CA, Choi YH, Hagedorn CH, Brenner D. Replicative senescence of activated human hepatic stellate cells is accompanied by a pronounced inflammatory but less fibrogenic phenotype. Hepatology. 2003;37(3):653–664.

77. Bachem MG, Meyer D, Melchior R, Sell KM, Gressner AM. Activation of rat liver perisinusoidal lipocytes by transforming growth factors derived from myofibroblastlike cells. A potential mechanism of self perpetuation in liver fibrogenesis. J Clin Invest. 1992;89(1):19–27.

78. Bachem MG, Meyer D, Schäfer W, Riess U, Melchior R, Sell KM, et al. The response of rat liver perisinusoidal lipocytes to polypeptide growth regulator changes with their transdifferentiation into myofibroblast-like cells in culture. Journal of hepatology. 1993;18(1):40–52.

79. Dooley S, Delvoux B, Lahme B, Mangasser-Stephan K, Gressner AM. Modulation of transforming growth factor β response and signaling during transdifferentiation of rat hepatic stellate cells to myofibroblasts. Hepatology. 2000;31(5):1094–1106.

80. Friedman SL, Yamasaki G, Wong L. Modulation of transforming growth factor beta receptors of rat lipocytes during the hepatic wound healing response. Enhanced binding and reduced gene expression accompany cellular activation in culture and in vivo. Journal of Biological Chemistry. 1994;269(14):10551–10558.

81. Vilar JMG, Jansen R, Sander C. Signal processing in the TGF-β superfamily ligand-receptor network. PLoS computational biology. 2006;2(1):e3.

82. Montosi G, Garuti C, Iannone A, Pietrangelo A. Spatial and temporal dynamics of hepatic stellate cell activation during oxidant-stress-induced fibrogenesis. Am J Pathol. 1998;152(5):1319–1326.

83. Liu X, Xu J, Brenner DA, Kisseleva T. Reversibility of liver fibrosis and inactivation of fibrogenic myofibroblasts. Current pathobiology reports. 2013;1(3):209–214.

84. Marvie P, Lisbonne M, L'helgoualc'h A, Rauch M, Turlin B, Preisser L, et al. Interleukin-33 overexpression is associated with liver fibrosis in mice and humans. J Cell Mol Med. 2010;14(6B):1726–1739.

85. Gailhouste L, Le Grand Y, Odin C, Guyader D, Turlin B, Ezan F, et al. Fibrillar collagen scoring by second harmonic microscopy: a new tool in the assessment of liver fibrosis. Journal of hepatology. 2010;52(3):398–406.

86. Subramanian A, Tamayo P, Mootha VK, Mukherjee S, Ebert BL, Gillette MA, et al. Gene set enrichment analysis: a knowledge-based approach for interpreting genome-wide expression profiles. Proc Natl Acad Sci U S A. 2005;102(43):15545–15550.

87. Mootha VK, Lindgren CM, Eriksson KF, Subramanian A, Sihag S, Lehar J, et al. PGC-1alpha-responsive genes involved in oxidative phosphorylation are coordinately downregulated in human diabetes. Nat Genet. 2003;34(3):267–273.

88. Martin FJ, Amode MR, Aneja A, Austine-Orimoloye O, Azov AG, Barnes I, et al. Ensembl 2023. Nucleic Acids Res. 2023;51(D1):D933–D941.

89. Love MI, Huber W, Anders S. Moderated estimation of fold change and dispersion for RNA-seq data with DESeq2. Genome biology. 2014;15(12):1–21.

90. Denning PJ, Lewis TG. Exponential laws of computing growth. Communications of the ACM. 2016;60(1):54–65.

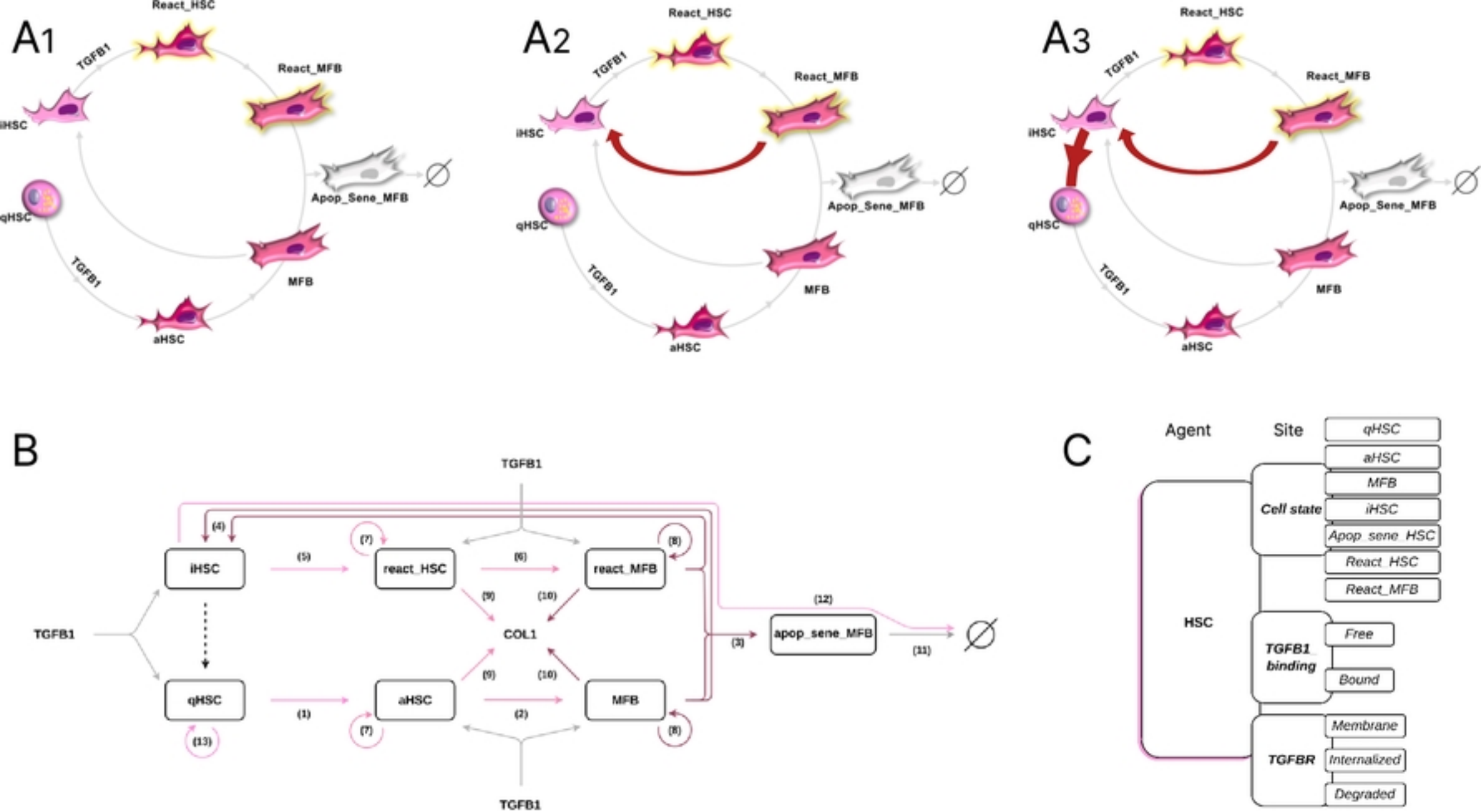
A1
A2
A3
React_HSC
React_MFB
Apop_Sene_MFB
MFB
aHSC
qHSC
iHSC
TGFB1
B
TGFB1
iHSC
react_HSC
react_MFB
COL1
apop_sene_MFB
qHSC
aHSC
MFB
(1)
(2)
(3)
(4)
(5)
(6)
(7)
(8)
(9)
(10)
(11)
(12)
(13)
C
Agent
Site
HSC
Cell state
qHSC
aHSC
MFB
iHSC
Apop_sene_HSC
React_HSC
React_MFB
TGFB1 binding
Free
Bound
TGFBR
Membrane
Internalized
Degraded

Figure 1

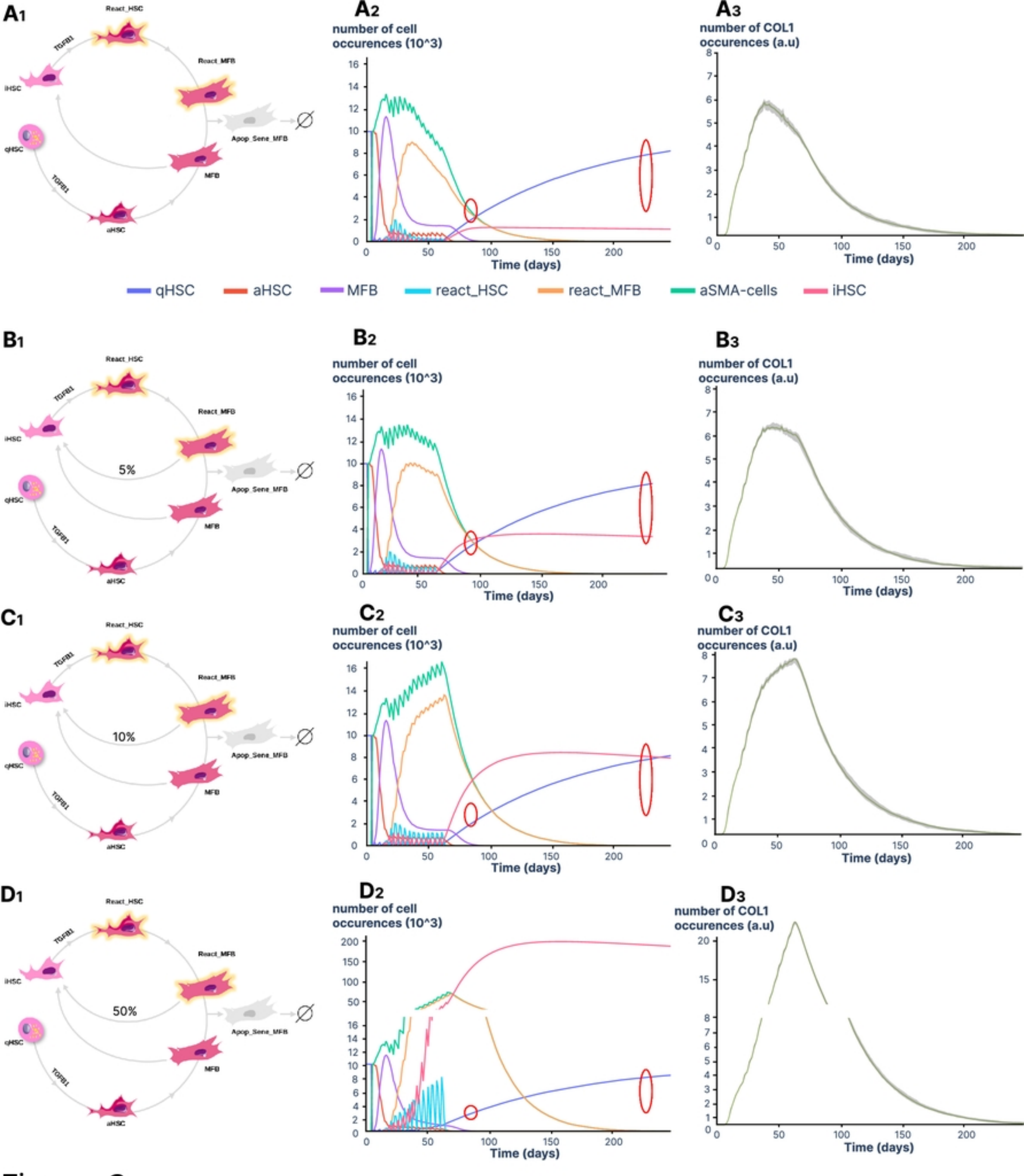
A1
B1
C1
D1
React_HSC
React_MFB
Apop_Sene_MFB
MFB
aHSC
qHSC
iHSC
TGFB1
5%
10%
50%
A2
B2
C2
D2
number of cell occurences (10^3)
Time (days)
A3
B3
C3
D3
number of COL1 occurences (a.u)
qHSC
aHSC
MFB
react_HSC
react_MFB
aSMA-cells
iHSC

Figure 2

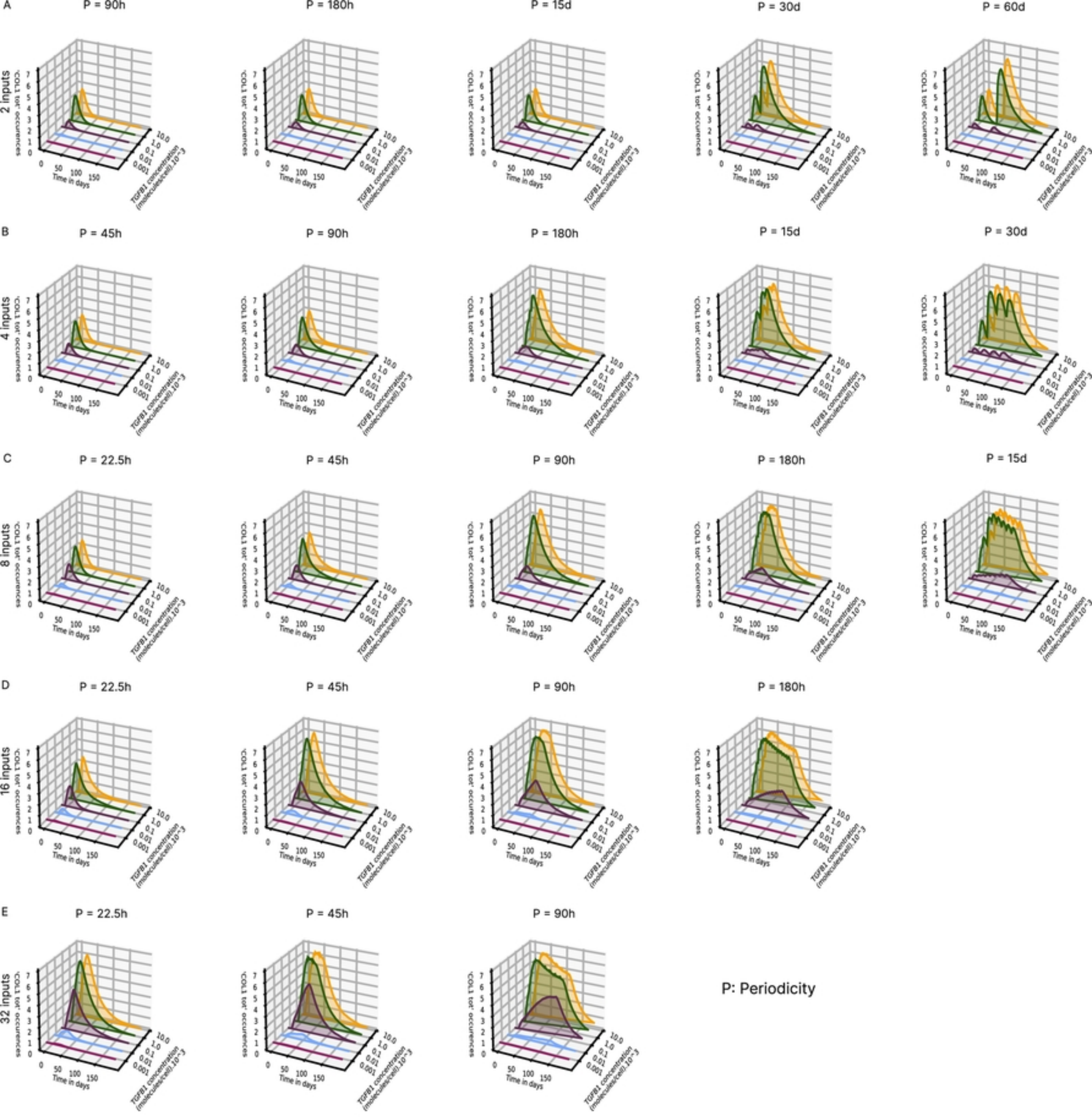
A
P = 90h
P = 180h
P = 15d
P = 30d
P = 60d
2 inputs
B
P = 45h
P = 90h
P = 180h
P = 15d
P = 30d
4 inputs
C
P = 22.5h
P = 45h
P = 90h
P = 180h
P = 15d
8 inputs
D
P = 22.5h
P = 45h
P = 90h
P = 180h
16 inputs
E
P = 22.5h
P = 45h
P = 90h
32 inputs
'COL1 tot' occurences
Time in days
TGFB1 concentration (molecules/cell).10^-3
P: Periodicity

Figure 3

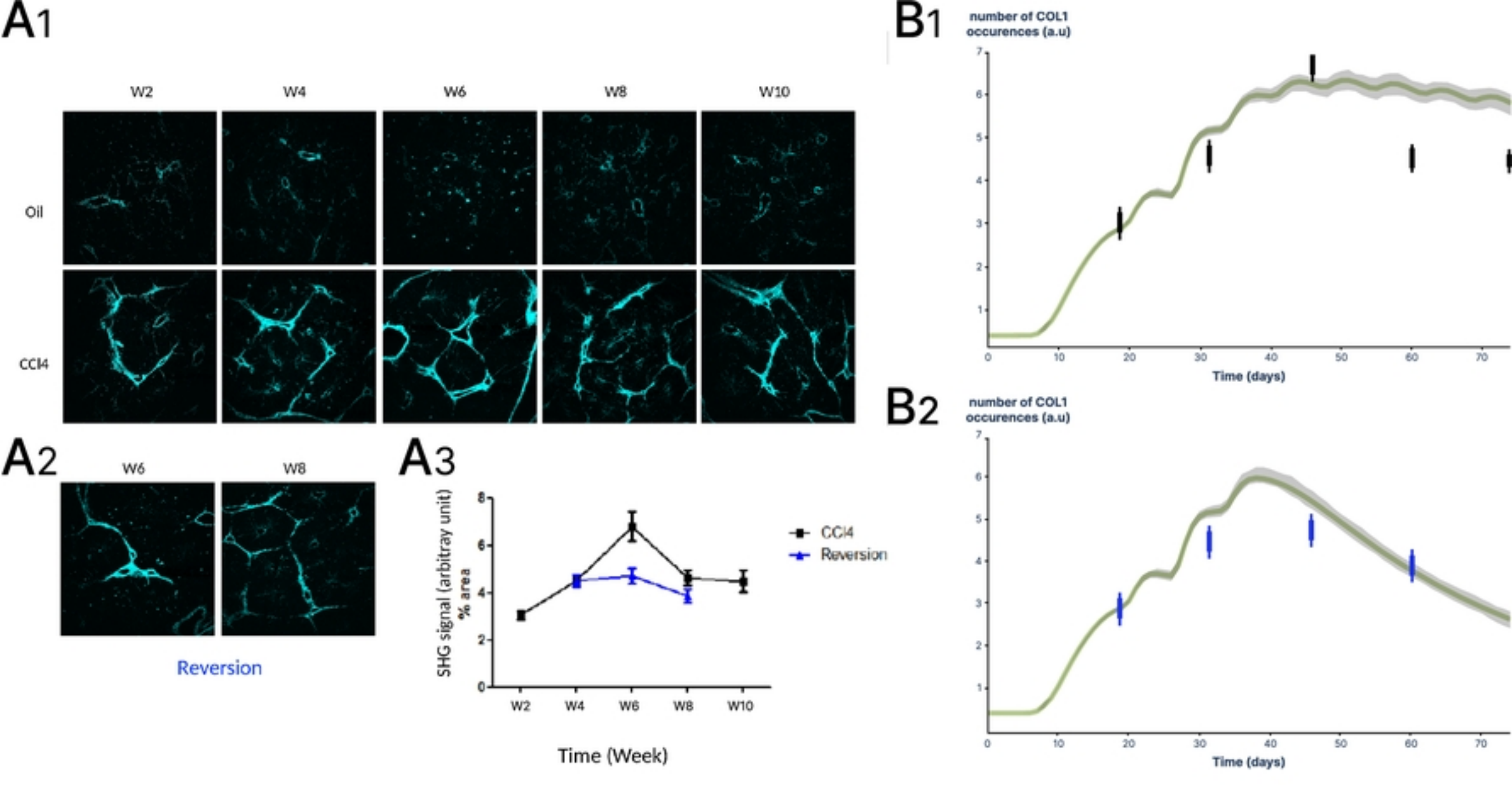
A1
W2
W4
W6
W8
W10
Oil
CCl4
A2
W6
W8
Reversion
A3
SHG signal (arbitray unit)
% area
CCl4
Reversion
W2
W4
W6
W8
W10
Time (Week)
B1
number of COL1
occurences (a.u)
Time (days)
B2
number of COL1
occurences (a.u)
Time (days)

Figure 4

A

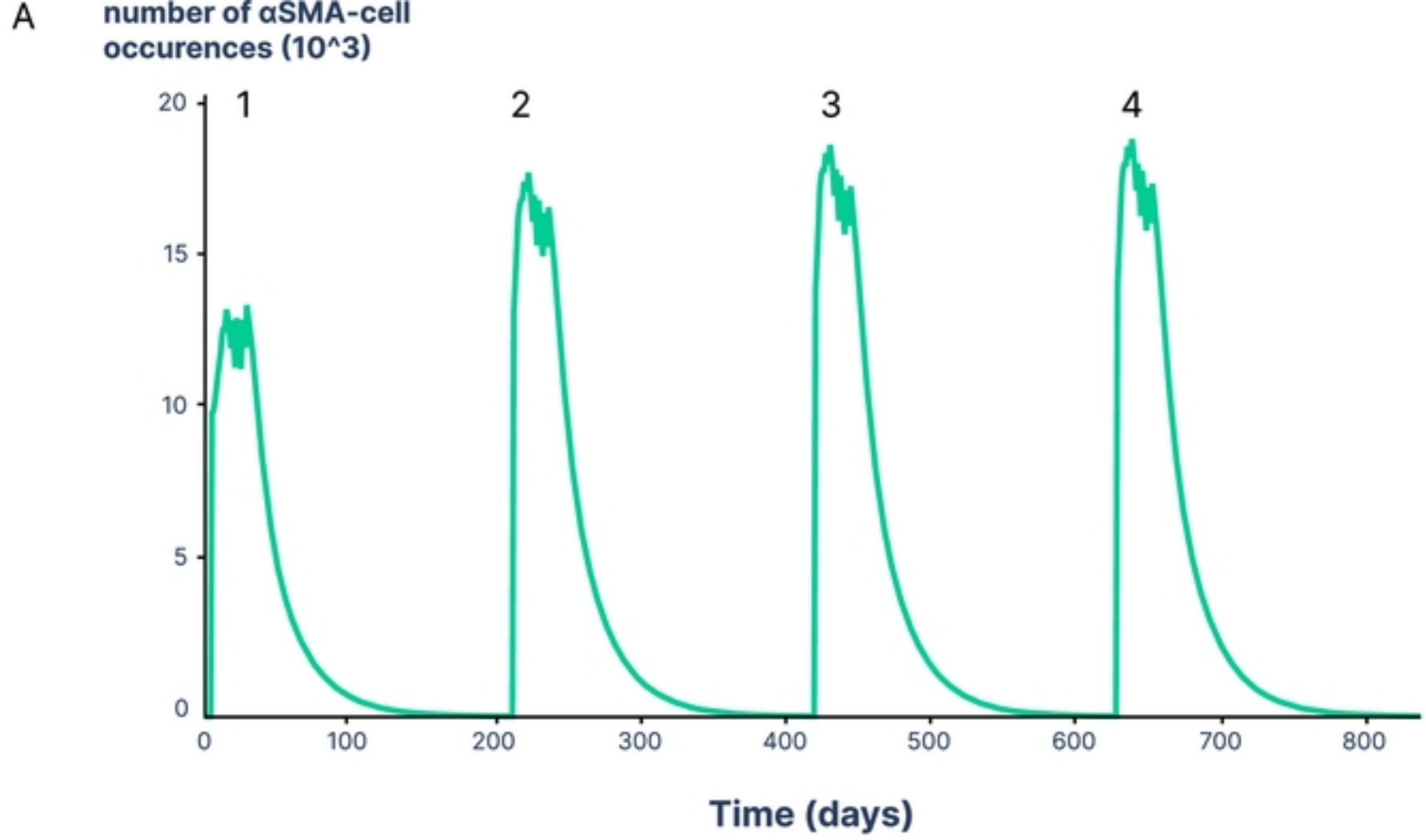
number of αSMA-cell occurences (10^3)
1
2
3
4
20
15
10
5
0
0
100
200
300
400
500
600
700
800
Time (days)

B

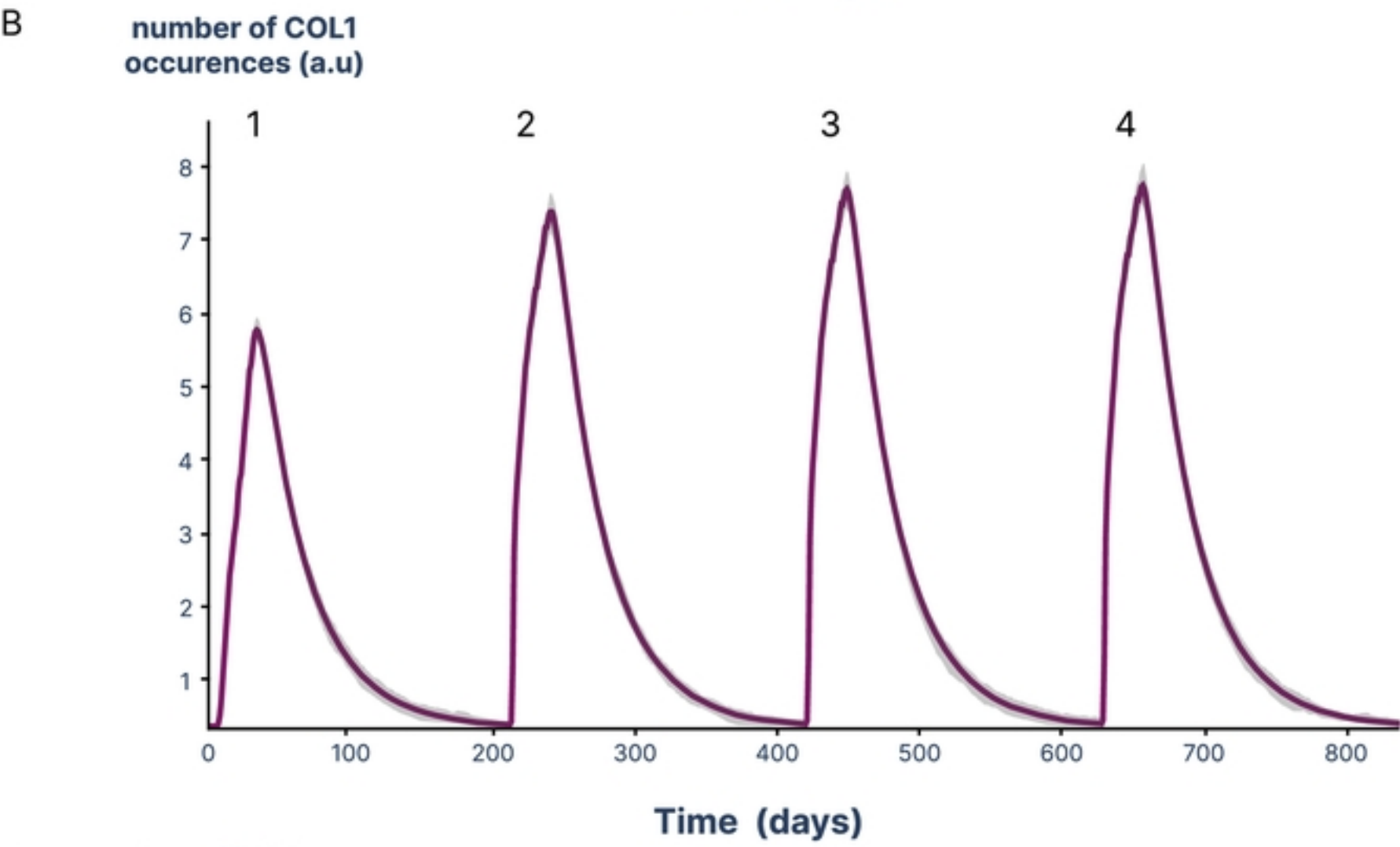
number of COL1 occurences (a.u)
1
2
3
4
8
7
6
5
4
3
2
1
0
100
200
300
400
500
600
700
800
Time (days)

C

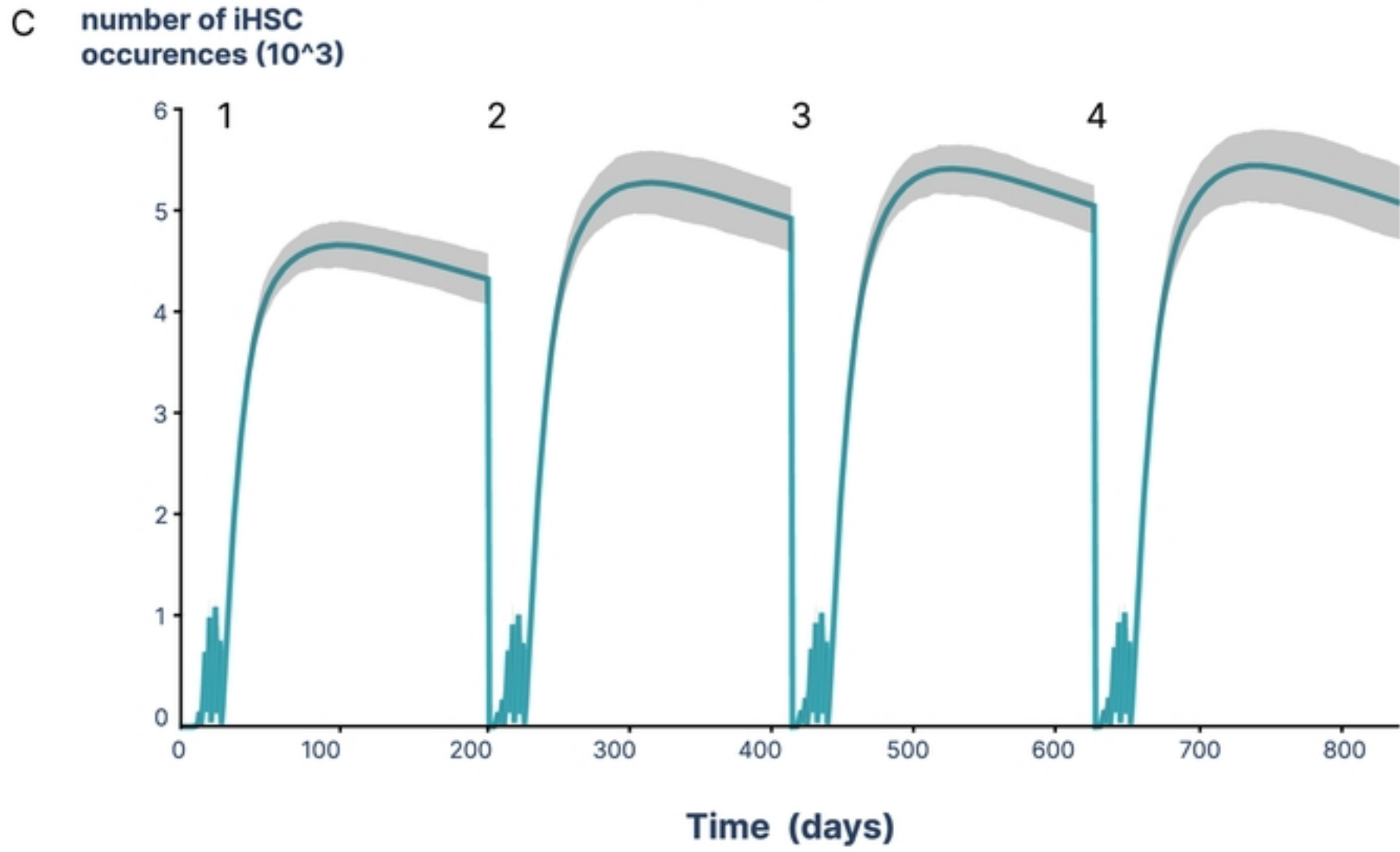
number of iHSC occurences (10^3)
1
2
3
4
6
5
4
3
2
1
0
0
100
200
300
400
500
600
700
800
Time (days)

Figure 5

A

Enrichment Score (ES): 0.4256573

Normalized Enrichment Score (NES) 1.3889463

Nominal p-value: 0.097247705

FWER p-Value: 0.053

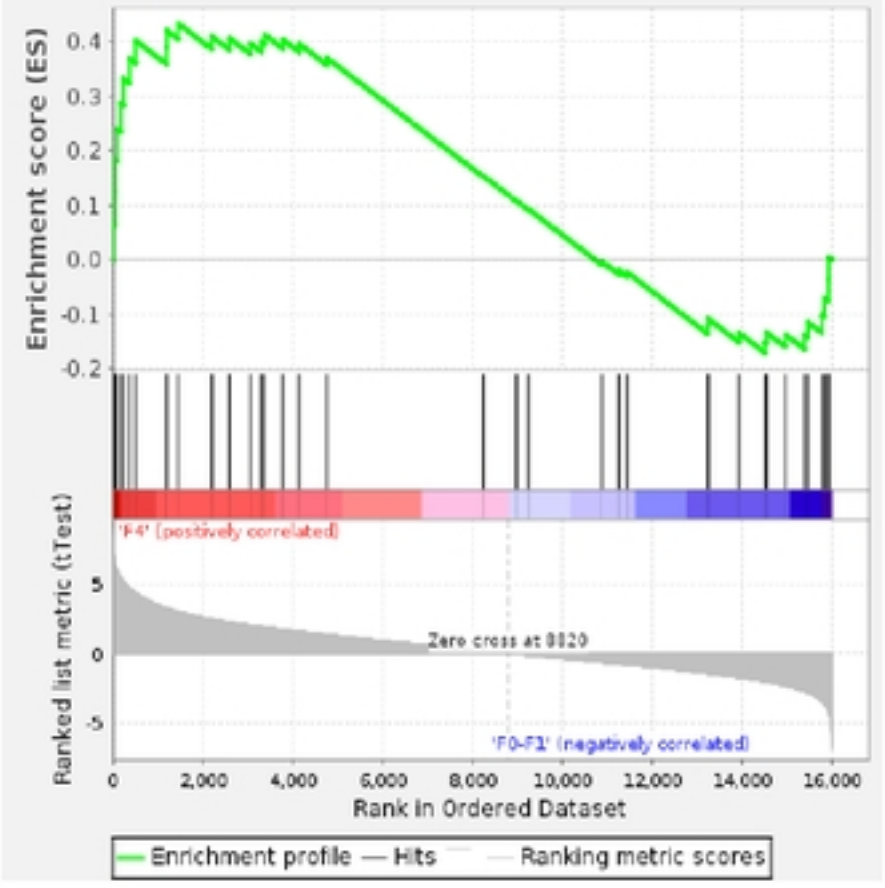

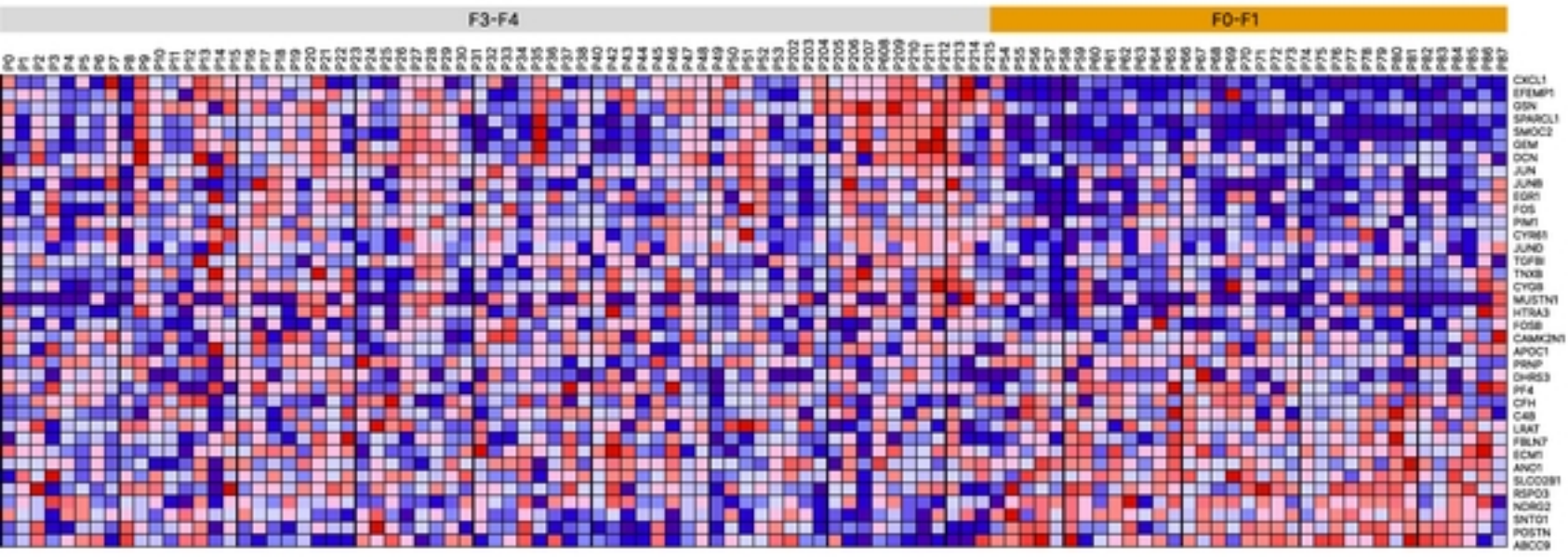

B

Enrichment Score (ES): 0.46911344

Normalized Enrichment Score (NES) 1.5760338

Nominal p-value: 0.04789272

FWER p-Value: 0.025

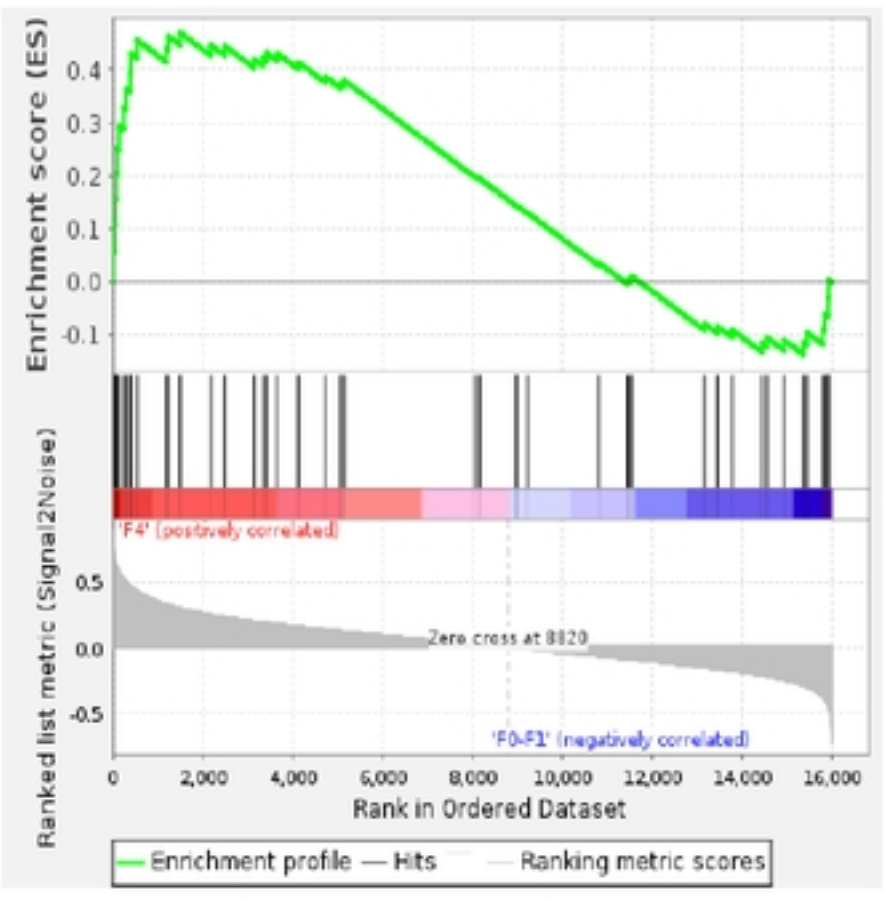

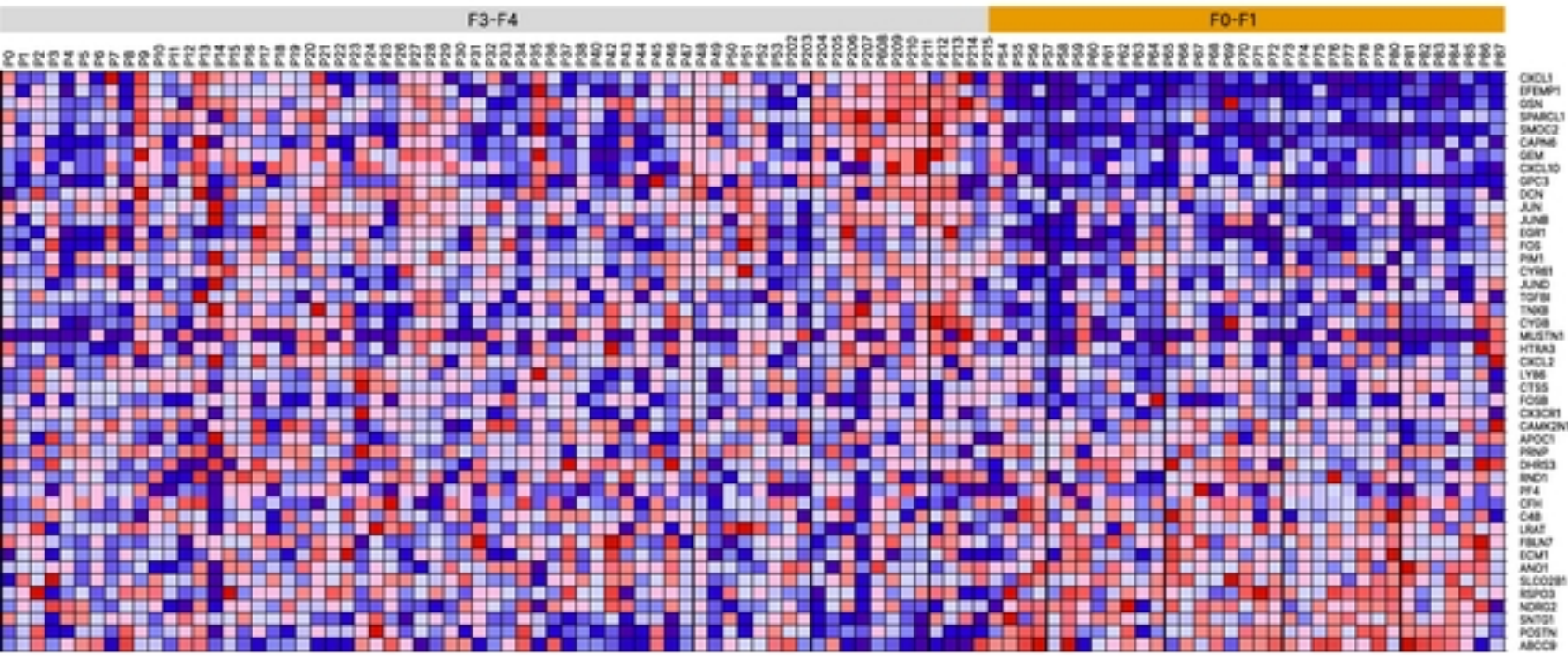

Figure 6

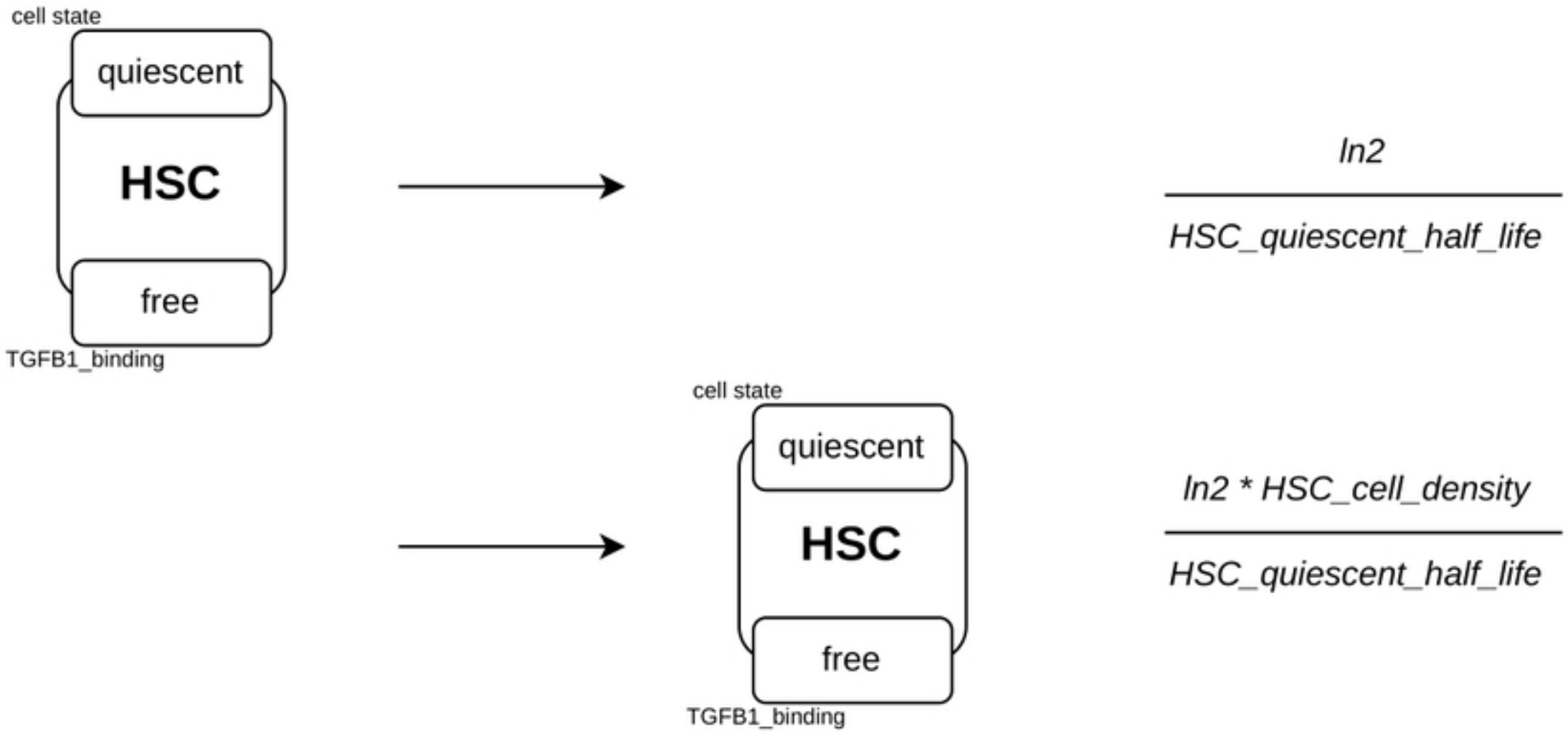
cell state
quiescent
HSC
free
TGFB1_binding
ln2
HSC_quiescent_half_life
cell state
quiescent
HSC
free
TGFB1_binding
ln2 * HSC_cell_density
HSC_quiescent_half_life

Figure 7

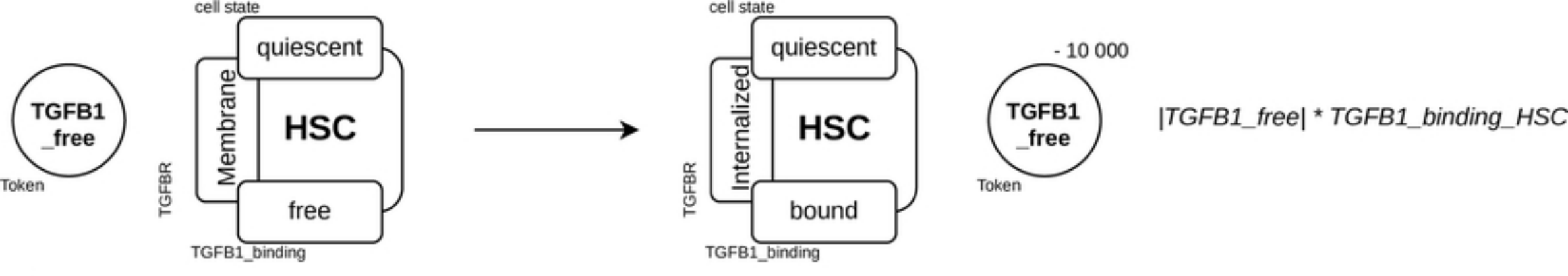
cell state
quiescent
Membrane
HSC
free
TGFBR
TGFB1_binding
TGFB1
_free
Token
cell state
quiescent
Internalized
HSC
bound
TGFBR
TGFB1_binding
- 10 000
TGFB1
_free
Token
|TGFB1_free| * TGFB1_binding_HSC

Figure 8

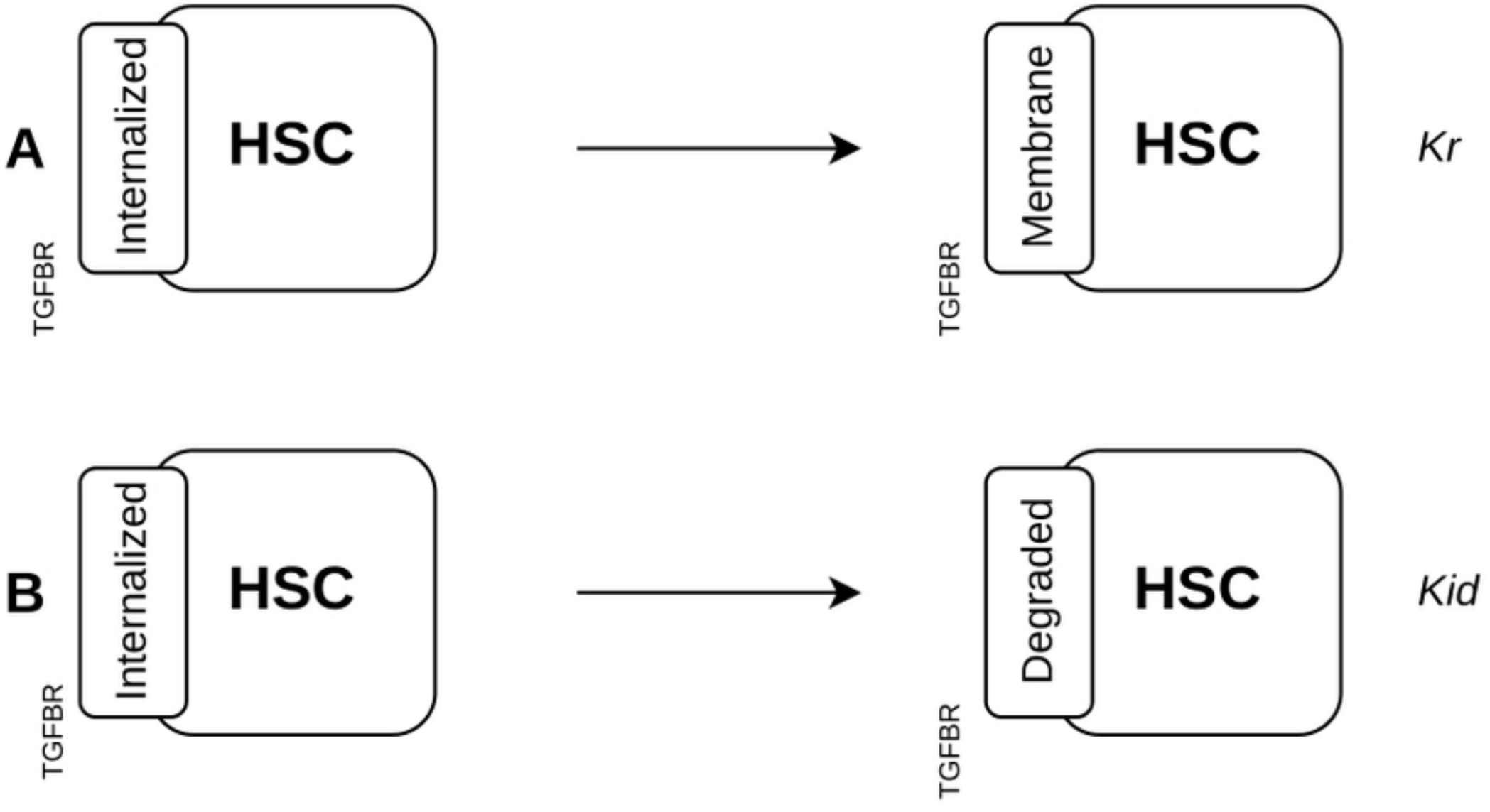
A
Internalized
HSC
TGFBR
Membrane
HSC
TGFBR
Kr
B
Internalized
HSC
TGFBR
Degraded
HSC
TGFBR
Kid

Figure 9

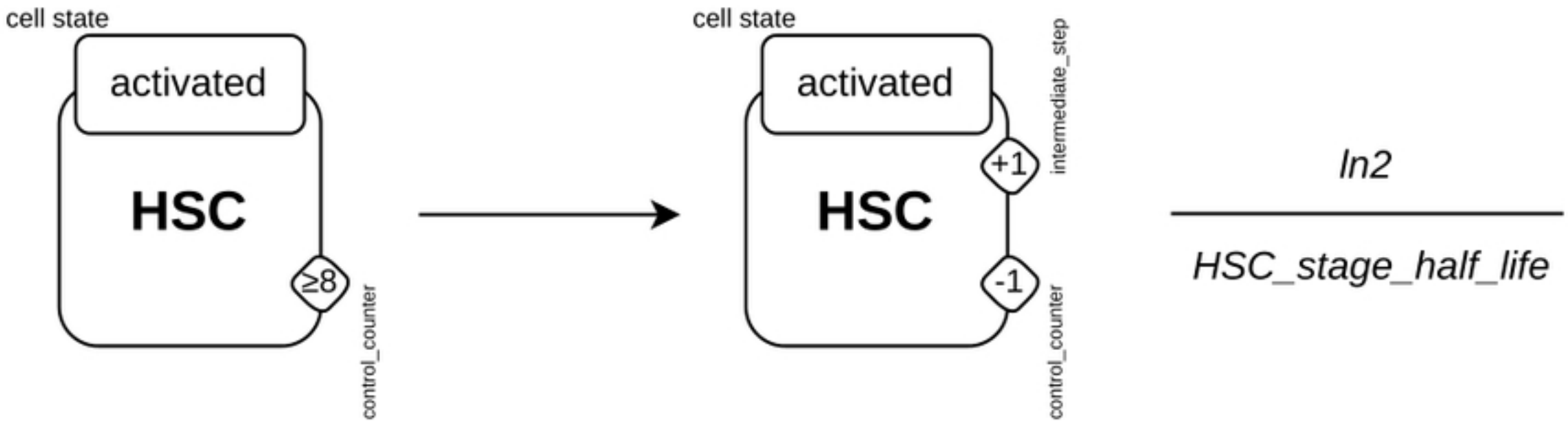
cell state
activated
HSC
≥8
control_counter
cell state
activated
HSC
+1
-1
intermediate_step
control_counter
ln2
HSC_stage_half_life

Figure 10

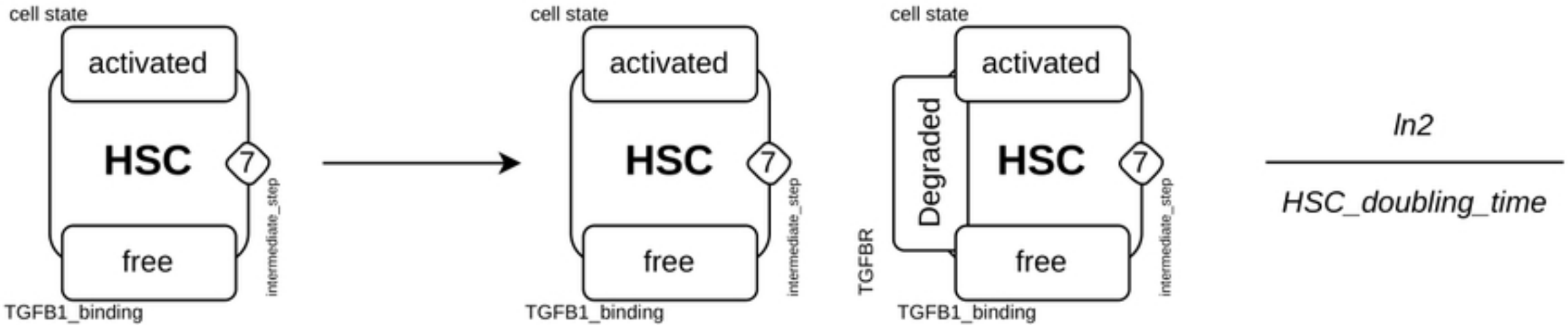
cell state
activated
HSC
7
free
intermediate_step
TGFB1_binding
cell state
activated
HSC
7
free
intermediate_step
TGFB1_binding
cell state
activated
Degraded
HSC
7
free
TGFBR
intermediate_step
TGFB1_binding
ln2
HSC_doubling_time

Figure 11

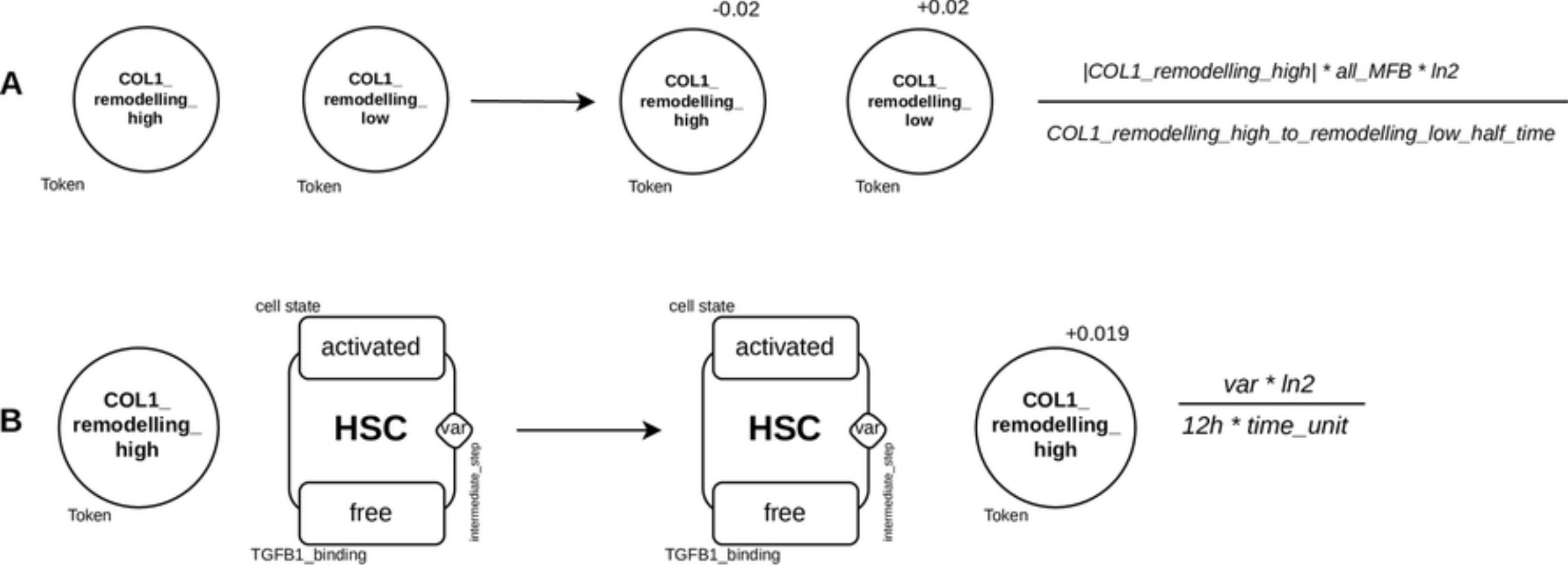
A
COL1_ remodelling_ high
Token
COL1_ remodelling_ low
Token
-0.02
COL1_ remodelling_ high
Token
+0.02
COL1_ remodelling_ low
Token
|COL1_remodelling_high| * all_MFB * ln2
COL1_remodelling_high_to_remodelling_low_half_time
B
COL1_ remodelling_ high
Token
cell state
activated
HSC
var
free
intermediate_step
TGFB1_binding
cell state
activated
HSC
var
free
intermediate_step
TGFB1_binding
+0.019
COL1_ remodelling_ high
Token
var * ln2
12h * time_unit

Figure 12

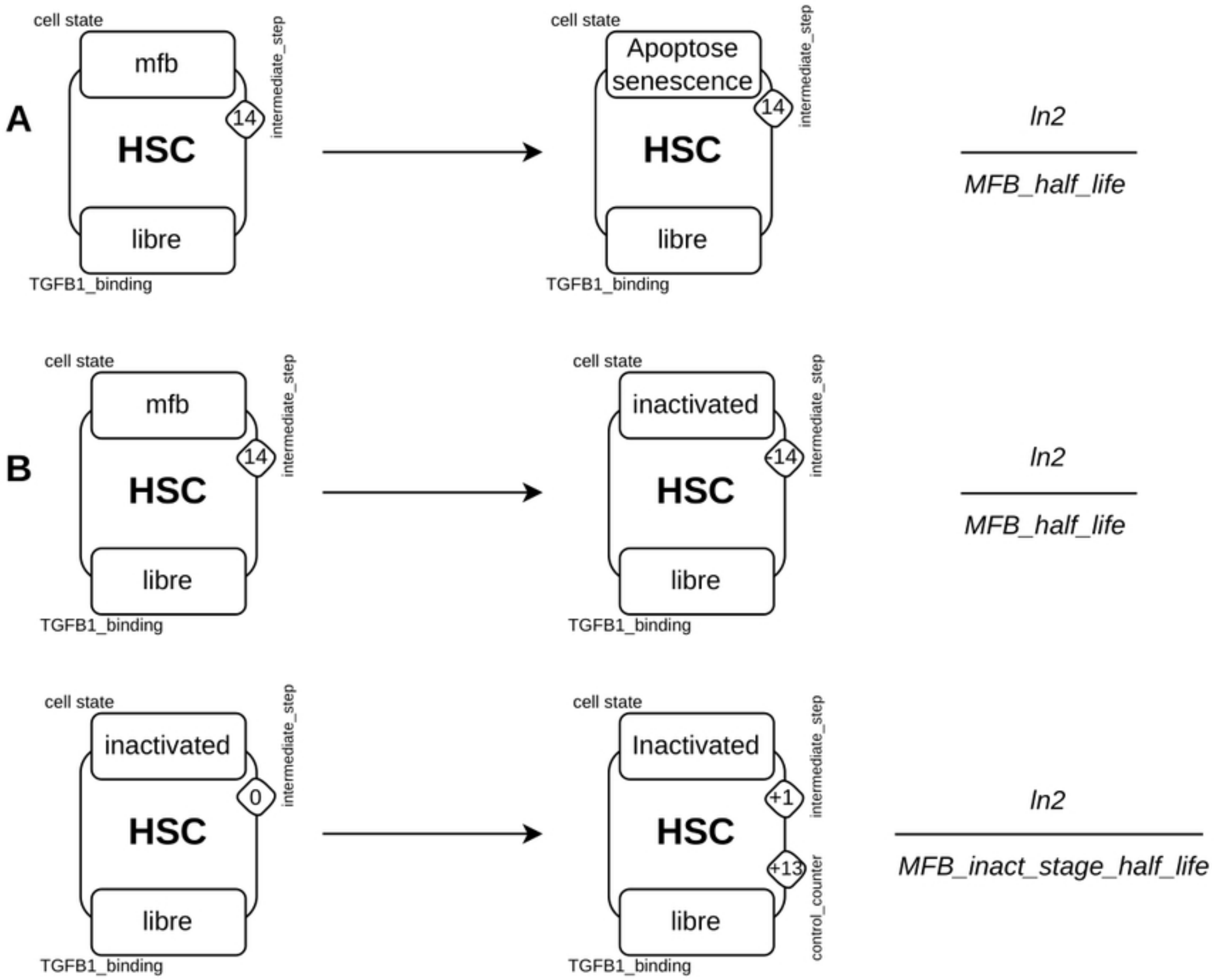
A
cell state
mfb
HSC
libre
TGFB1_binding
14
intermediate_step
cell state
Apoptose senescence
HSC
libre
TGFB1_binding
14
intermediate_step
ln2
MFB_half_life
B
cell state
mfb
HSC
libre
TGFB1_binding
14
intermediate_step
cell state
inactivated
HSC
libre
TGFB1_binding
14
intermediate_step
ln2
MFB_half_life
cell state
inactivated
HSC
libre
TGFB1_binding
0
intermediate_step
cell state
Inactivated
HSC
libre
TGFB1_binding
+1
intermediate_step
+13
control_counter
ln2
MFB_inact_stage_half_life

Figure 13